Backbone and Side Chain Dynamics of Uncomplexed Human Adipocyte and Muscle Fatty Acid-Binding Proteins

Keith L. Constantine,*,‡ Mark S. Friedrichs,‡ Michael Wittekind,‡ Haris Jamil,§ Ching-Hsuen Chu,§ Rex A. Parker,§ Valentina Goldfarb,‡ Luciano Mueller,‡ and Bennett T. Farmer, II‡

Department of Macromolecular NMR and Department of Metabolic Diseases, Bristol-Myers Squibb Pharmaceutical Research Institute, Princeton, New Jersey 08543-4000

Received January 27, 1998; Revised Manuscript Received March 25, 1998

ABSTRACT: Adipocyte lipid-binding protein (A-LBP) and muscle fatty acid-binding protein (M-FABP) are members of a family of small (∼15 kDa) cytosolic proteins that are involved in the metabolism of fatty acids and other lipid-soluble molecules. Although highly homologous (65%) and structurally very similar, A-LBP and M-FABP display distinct ligand binding characteristics. Since ligand binding may be influenced by intrinsic protein dynamical properties, we have characterized the backbone and side chain dynamics of uncomplexed (apo) human A-LBP and M-FABP. Backbone dynamics were characterized by measurements of ^{15}N T_1 and T_2 values and $\{^1H\}-^{15}N$ NOEs. These data were analyzed using model-free spectral density functions and reduced spectral density mapping. The dynamics of methyl-containing side chains were charaterized by measurements of ^2H T_1 and $T_{1\rho}$ relaxation times of $^{13}C^1H_2{}^2H$ groups. The ^2H relaxation data were analyzed using the model-free approach. For A-LBP, ^{15}N relaxation data were obtained for 111 residues and ^2H relaxation data were obtained for 42 methyl groups. For M-FABP, ^{15}N relaxation data were obtained for 111 residues and ^2H relaxation data were obtained for 53 methyl groups. The intrinsic flexibilities of these two proteins are compared, with particular emphasis placed on binding pocket residues. There are a number of distinct dynamical differences among corresponding residues between the two proteins. In particular, many residues display greater backbone picosecond to nanosecond and/or microsecond to millisecond time scale mobility in A-LBP relative to M-FABP, including F57, K58, and most residues in α-helix 2 (residues 28−35). Variations in the dynamics of this region may play a role in ligand selectivity. The side chains lining the fatty acid binding pocket display a wide range of motional restriction in both proteins. Side chains showing distinct dynamical differences between the two proteins include those of residues 20, 29, and 51. This information provides a necessary benchmark for determining dynamical changes induced by ligand binding and may ultimately lead to an enhanced understanding of ligand affinity and selectivity among fatty acid-binding proteins.

Adipocyte lipid-binding protein (A-LBP)[1] and muscle fatty acid-binding protein (M-FABP) are members of a family of intracellular lipid-binding proteins (iLBPs; reviewed in ref *1*). Although the precise metabolic roles played by these proteins are unclear, they are involved in the transport and storage of lipids. A-LBP occurs in fat cells, while M-FABP occurs in skeletal muscle, heart, kidney, and other tissues.

Although A-LBP and M-FABP have relatively high sequence homology (65%; see Figure 1) and similar tertiary structures, including similar ligand binding pockets, the two proteins have distinct ligand binding charateristics (*2*, *3*). For example, M-FABP binds stearic acid with a 30−40-fold higher affinity compared to A-LBP (*2*). In addition, A-LBP and M-FABP display markedly different modes of long chain fatty acid binding: A-LBP binds fatty acids in a slightly bent U-shaped conformation (*4*), whereas M-FABP binds fatty acids in a U-shaped conformation (*5*). To more fully understand the factors that may influence ligand binding and

```
                10        20        30        40        50
A-LBP     CDAFVGTWKLVSSENFDDYMKEVGVGFATRKVAGMAKPNMIISVNGDVIT
M-FABP  MV---L------D-K-------SL-------Q--S-T--TT--EK---IL-

                60        70        80        90        100
A-LBP     IKSESTFKNTEISFILGQEFDEVTADDRKVKSTITLDGGVLVHVQKWDGK
M-FABP    L-TH----------K--V----T---------IV-----K---L-----Q

                110       120       130
A-LBP     STTIKRKREDDKLVVECVMKGVTSTRVYERA
M-FABP    E--LV-ELI-G--ILTLTHGTAVC--T--KEA
```

FIGURE 1: Amino acid sequences of human A-LBP and human M-FABP. The complete sequence of A-LBP is shown. For M-FABP, a dash (−) is used for conserved residues; residues differing from those found in A-LBP are shown explicitly.

* To whom correspondence should be addressed.
‡ Department of Macromolecular NMR.
§ Department of Metabolic Diseases.

[1] Abbreviations: A-LBP, adipocyte lipid-binding protein; CPMG, Carr−Purcell−Meiboom−Gill; DNA, deoxyribonucleic acid; DTT, dithiothreitol; EDTA, ethylenediaminetetraacetate; FABP, fatty acid-binding protein; FID, free induction decay; HSQC, heteronuclear single-quantum coherence; I-FABP, intestinal FABP; iLBP, intracellular lipid-binding protein; IPTG, isopropyl thiogalactoside; M-FABP, muscle FABP; NMR, nuclear magnetic resonance; NOE, nuclear Overhauser effect; OD, optical density; PFG, pulsed field gradient; ppm, parts per million; RF, radio frequency; rms, root-mean-square; SDS−PAGE, sodium dodecyl sulfate−polyacrylamide gel electrophoresis; TOCSY, total correlation spectroscopy; 2D, two-dimensional; 3D, three-dimensional.

S0006-2960(98)00203-7 CCC: $15.00
Published on Web 05/19/1998

selectivity, we have conducted NMR relaxation studies of the apo forms of human A-LBP and M-FABP. Recent studies of intestinal FABP (I-FABP; *6*) and ileal lipid-binding protein (*7*) indicate that protein flexibility may play an important role in ligand affinity and selectivity for iLBPs.

The physical basis for ligand selectivity may arise from both protein structural and dynamic differences. While structural differences are obvious starting points for identifying selectivity-enhancing features, the potential consequences of differences in protein dynamics are more abstruse. Nevertheless, two recent publications indicate that the intrinsic flexibilities of protein binding site residues, i.e., the distributions of accessible conformational substates (*8*) in the absence of bound ligands, are directly related to the conformational adaptability observed in various protein−ligand complexes. The first article (*9*) describes a study by X-ray crystallography and hydrogen exchange of the binding of a set of ligands to a cavity-containing mutant of T4 lysozyme. Residues in the apoprotein showing high temperature factors and rapid hydrogen exchange were able to adopt different conformations in response to different ligands, whereas residues characterized by low temperature factors and slow hydrogen exchange remained fixed in response to different ligands. In the second article (*10*), the 120 K X-ray structure of apo-α-lytic protease at 1.5 Å resolution was characterized by a multiconformational refinement procedure, and the results were compared to X-ray structures of the enzyme complexed to a variety of inhibitors. Quoting the authors, "The active site residues that are perturbed during accommodation of different substrates are precisely those showing conformational substates, implying that substrate binding selects a subset of conformations from the ensemble of accessible states."

These results suggest that so-called "induced fit" binding modes (*11*) may often be more accurately described as "selected fit" binding modes. Induced fit, consistently defined, involves forcing the protein to adopt a bound-state conformation that is inaccessible to the apoprotein, whereas selected fit involves stabilizing an accessible conformation. Selected fit has also been termed a "ligand-coupled conformational equilibrium" (*12*), wherein ligand binding shifts a pre-existing conformational equilibrium. Induced fit will generally have an unfavorable enthalpic cost (steric hindrance) relative to a selected fit. Although a selected fit will entail a reduction in the conformational entropy of the protein, this may be a relatively small component of the overall free energy in many cases (*13*). Unfavorable steric clashes are more likely to occur in the rigid regions of a binding site. Thus, dynamic properties may play a role in ligand selectivity by allowing additional variability in those ligand moieties that interact with flexible portions of the binding site (*9*). Differences in the distributions of flexible and rigid residues between homologous binding sites may account, in part, for differential selectivity.

Among the methods available for characterizing solution-state protein conformational dynamics, only NMR relaxation measurements can provide detailed experimental information for a great variety of sites within a protein. The determination of ^{15}N NMR relaxation parameters has become widely used in the characterization of protein backbone dynamics (e.g., see refs *6* and *14*−*21*). Most commonly, ^{15}N longitudinal relaxation rates (R_1), ^{15}N transverse relaxation rates

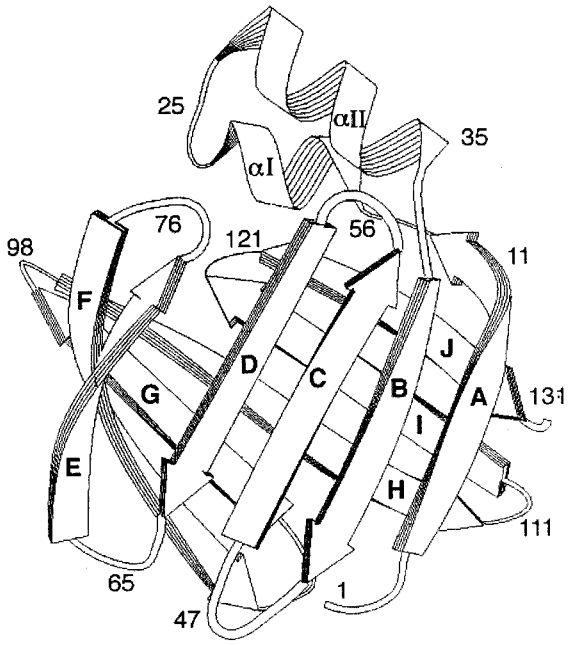

FIGURE 2: Ribbon drawing of the backbone fold of A-LBP derived from the human A-LBP homology model (see the text). The β-strands (arrows), α-helices, and selected residue positions are labeled.

(R_2), and {^{1}H}−^{15}N nuclear Overhauser effects (NOEs) are fit to model-free spectral density functions (*22*−*25*), yielding information on picosecond to nanosecond time scale motions (N−H vector order parameters and local correlation times) and microsecond to millisecond time scale motions (exchange contributions to R_2). Alternatively, linear combinations of ^{15}N NMR relaxation parameters can be used to obtain the values of "reduced" spectral density functions (*26*−*30*). The reduced spectral density approach has the advantage of not requiring any parameter selection criteria or least-squares fitting, but the dynamic information obtained is not as straightforward to interpret. Information on the picosecond to nanosecond time scale dynamics of methyl-containing side chains can be obtained using recently developed experiments (*31*, *32*) for measuring ^{2}H relaxation parameters. Specifically, ^{2}H R_1 and rotating frame ($R_{1\rho}$) relaxation rates are obtained and fit to a model-free spectral density function, yielding methyl axis order parameters and internal correlation times.

For uncomplexed (apo) human A-LBP and M-FABP, we have measured both backbone ^{15}N and side chain methyl group ^{2}H relaxation parameters. These proteins share the common iLBP fold (Figure 2; reviewed in ref *1*), which is composed of 10 antiparallel β-strands (designated A−J) and a helix−loop−helix motif connecting β-strands A and B. The lipid-binding cavity encompasses an area extending from near the center of the protein to the internal faces of α-helices I and II. The cavity is lined by both polar and nonpolar residues, including a number with methyl-containing side chains. Thus, methyl group ^{2}H relaxation affords dynamical information on moieties that are likely to interact directly with bound ligands.

In this article, the backbone and side chain dynamics of apo-A-LBP and apo-M-FABP are compared, and potential correlations between the dynamical properties and structural features are explored. The backbone dynamics data of these

proteins are also compared to the data given in a recently reported ^{15}N relaxation study (*6*) of apo-I-FABP. Finally, the implications of these results for iLBP ligand binding and selectivty are discussed.

EXPERIMENTAL PROCEDURES

Protein Expression and Purification. The recombinant A-LBP and M-FABP proteins were prepared first by subcloning the respective cDNA sequence into the pET11a expression vector and then by transforming *Escherichia coli* BL21(DE3) cells with that vector. Transformed cells were grown in 500 mL aliquots at 37 °C in minimal medium, containing both $(NH_4)_2SO_4$ and glucose, to an OD_{600} of ~0.6. For ^{15}N-labeled protein, $[^{15}N](NH_4)_2SO_4$ (Isotec) and unlabeled glucose were added to the 100% H_2O minimal medium. For ^{13}C- and ^{15}N-labeled protein, $[^{15}N](NH_4)_2SO_4$ and [$^{13}C_7$]-glucose (CIL) were added to the 100% H_2O minimal medium. For the 50% fractionally deuterated ^{13}C- and ^{15}N-labeled protein, $[^{15}N](NH_4)_2SO_4$ and [$^{13}C_7$]glucose were added to the 50% D_2O/50% H_2O (v/v) minimal medium.

The cells were then induced with 0.2 mM IPTG for 2 h at 37 °C and subsequently harvested by centrifugation at 4 °C. The cell pellet was resuspended in 100 mL of chilled 50 mM Tris-HCl, 100 mM NaCl, 10 mM EDTA, pH 7.5 buffer and then sonicated at 4 °C for 10 min in pulse mode to minimize heating. All subsequent steps were carried out at room temperature. The homogenate was spun down for 20 min at 15 000 rpm and then applied to a MacroPrep-Q column (Bio-Rad) equilibrated with the same resuspension buffer. A-LBP (M-FABP) protein comes out in the flow-through fraction. The flow-through fraction was then applied to a column of Reactive Red 120 dye resin (40 mL, Sigma) equilibrated with the same resuspension buffer. The flow-through fraction was collected, saturated to 40% with ammonium sulfate, and then stirred on ice for 30 min. Any precipitate was removed by centrifugation. The supernatant was applied to a 50 mL column of Phenyl-Sepharose 6 (Pharmacia) and washed with 40% ammonium sulfate in 50 mM Tris-HCl, pH 7.5 buffer until the effluent showed an OD_{280} of ~0.01. A-LBP (M-FABP) was then eluted with 20% ammonium sulfate until the effluent showed an OD_{280} of ~0.02. The protein solution was concentrated to 5 mL using an Amicon concentrator equipped with a YM3 membrane. At this stage, the protein is ~95 to 97% pure as determined by SDS−PAGE. The concentrated protein solution was then loaded onto a Superdex 30 16/60 column (Pharmacia) equilibrated with 50 mM NaP_i and 150 mM NaCl (pH 7.5).

For A-LBP, corresponding protein fractions from the Superdex column were first warmed to 37 °C and then applied to a prewarmed Lipidex 1000 column (Sigma) equilibrated with buffer containing 25 mM NaP_i, 50 mM NaCl, 1 mM EDTA, 0.1 mM NaN_3, and 10% D_2O at pH 7.5 (NMR buffer without DTT). The latter step is designed to remove bound lipids. The A-LBP protein was left on the Lipidex column for 2 h at 37 °C. After 2 h, the protein was washed off the Lipidex column using NMR buffer (with 5 mM DTT).

For M-FABP, corresponding protein fractions from the Superdex column were first warmed to 52 °C and then applied to a prewarmed Lipidex 1000 column (Sigma) equilibrated with NMR buffer without DTT. The M-FABP protein was left on the Lipidex column for 30 min at 52 °C. After 30 min, the protein was washed off the Lipidex column using NMR buffer (with 5 mM DTT). At this point, the protein solution (A-LBP and M-FABP) was concentrated to 3 mL on a Centriprep 3 concentrator (Amicon). The protein solution was further concentrated on a Centricon 3 concentrator (Amicon) and concomitantly exchanged with NMR buffer containing 5 mM deuterated DTT. All concentration steps were performed at room temperature. Typical yields for a 2 L growth were ~25 mg of highly pure protein.

NMR Sample Preparation. Protein samples for NMR experiments were concentrated to ~2.0 mM in buffers containing 25 mM NaP_i, 50 mM NaCl, 1 mM EDTA, 5 mM DTT, and 0.1 mM NaN_3 at pH 7.5 with 10% D_2O/90% H_2O (v/v). The samples were extensively degassed and transferred to 5 mm Shigemi restricted-volume NMR tubes, which were then closed under Ar.

NMR Data Acquisition and Processing. All NMR experiments were carried out at 20 °C either on a Varian Unity Plus 600 spectrometer (operating at a 599.91 MHz ^1H frequency) equipped with a Varian 5 mm $^1H/^{13}C/^{15}N$ triple-resonance, triple-axis PFG probe or on a Varian INOVA 600 spectrometer (operating at a 598.15 MHz ^1H frequency) equipped with a Varian 5 mm $^1H/^{13}C/^{15}N$ triple-resonance, singe-axis (*z*) PFG probe. All spectra were processed using a modified version of the FELIX program (Hare Research, Inc.; M. S. Friedrichs, unpublished), and the residual ^1H_2O signal was removed from all spectra by application of low-frequency deconvolution (*33*) in the ^1H acquisition dimension.

T_1(N) and T_2(N) were measured as previously described (*34*), with the following modifications. For the T_2 measurement, the ^{15}N CPMG pulse train was used with a pulse spacing of 0.8 ms ($\tau = 0.4$ ms in ref *34*). In all experiments, B_{0z} gradients (PFGs) have been employed for both artifact suppression (*35*) and coherence-transfer selection (*36*). Additionally, water-flipback pulses have been added as previously described for the HNCO and related experiments (*37*). Values for T_1(N) were measured using ^{15}N T_1 relaxation delays of 27.4, 52.4, 102.4, 152.4, 202.4, 302.4, 402.4, 502.4, 602.4, 852.4, and 1202.4 ms (11 time points); values for T_2(N) were measured using ^{15}N T_2 relaxation delays of 10.5, 20.9, 41.8, 62.8, 83.7, 94.1, 104.6, 115.1, 125.5, 156.9, and 198.7 ms (11 time points). T_1(N) and T_2(N) data were collected with eight transients per FID for a total acquisition time of 27 and 23 h, respectively.

The ^{15}N heteronuclear NOE was measured as described in ref *38* with the following pulse-sequence modifications: the $^{15}N \rightarrow {}^1H_N$ reverse INEPT transfer module was replaced with a gradient-enhanced, sensitivity-enhanced module (*36*), and two orthogonal RF purge pulses, SL_x and SL_y, were applied for a duration of 3.5 and 2.2 ms, respectively, immediately prior to the first ^{15}N 90° pulse. Proton saturation was achieved by a series of 125° ^1H pulses spaced at intervals of 5 ms during the entire relaxation delay of 8 s. No water-flipback pulses were employed. Twelve transients were collected per FID. FIDs with and without proton saturation were collected back to back for each component of the complex t_1 point. The total acquisition time was 28 h.

The time domain ^{15}N relaxation data were apodized with cosine-bell and Lorentzian/Gaussian resolution enhancement

functions in both the ^{1}H and ^{15}N dimensions. All data were Fourier transformed into real (ReRe) frequency-domain matrixes having a final size of 1024 × 1024. After Fourier transformation along t_2, only the downfield half (4.77−14.35 ppm) was retained in F_2, the ^{1}H acquisition dimension.

$T_1(H_zC_z)$, $T_1(H_zC_zD_z)$, and $T_{1\rho}(H_zC_zD_y)$ were measured as described by Kay and co-workers (*31*). Acquisition parameters were as follows: $t_{90}(^1H) = 5.9$ μs, $t_{90}(^{13}C) = 14.6$ μs, $t_{90}(^2H) = 119$ μs, $\gamma B_4(^2H) = 0.91$ kHz with WALTZ-16, $\gamma B_3(^{13}C) = 2.74$ kHz with WALTZ-16, $sw_1(^{13}C_{me}) = 4.51$ kHz, $t_{1max}(^{13}C_{me}) = 26.37$ ms, $sw(^1H) = 11.5$ kHz, $t_2 = 120$ ms, $\tau_a = 1.8$ ms, $\tau_b = 4.0$ ms, $\tau_c = 11.0$ ms, $T_C = 14.5$ ms, $g_{1z} = 32$ G/cm (1 ms), $g_{2y} = -6.1$ G/cm (0.5 ms), $g_{3z} = 25.6$ G/cm (0.5 ms), $g_{4z} = 12.8$ G/cm (0.5 ms), $g_{5z} = 27.8$ G/cm (0.8 ms), $g_{6z} = 15.0$ G/cm (0.5 ms), $g_{7y} = 6.9$ G/cm (0.6 ms) with a following delay of 2 ms, and $g_{8y} = 6.1$ G/cm (0.5 ms). All gradients g are specified by axis z or y, strength (gauss per centimeter), and duration (milliseconds). The phase cycle is given in ref *31*. The water resonance was selectively saturated with a 60 Hz ^{1}H RF field during both the general relaxation delay (1.2 s) and the ^{2}H relaxation mixing delay. A SCUBA sequence (*39*) was also inserted immediately prior to the first 90° proton pulse. The lock feedback loop was isolated from any incoming ^{2}H lock signal between the first proton 90° pulse and the start of the last τ_a delay. During this same time, the lock preamplifier was also gated off. When $T_{1\rho}(H_zC_zD_y)$ was measured, a ^{2}H spinlock was applied at an RF field strength of 1.3 kHz and a carrier frequency of ~1 ppm. $T_1(H_zC_zD_z)$ data were collected with eight transients per FID for a total acquisition time of 9 h; $T_{1\rho}(H_zC_zD_y)$ and $T_1(H_zC_z)$ data were collected with 16 transients per FID for total acquisition times of 16 and 18 h, respectively.

Values for $T_1(H_zC_z)$ were measured using ^{2}H relaxation delays of 5, 20, 40, 80, 120, 160, 200, 300, 400, and 600 ms (10 time points). Values for $T_1(H_zC_zD_z)$ were measured using ^{2}H relaxation delays of 5, 10, 20, 30, 40, 50, 60, 90, 120, and 200 ms (10 time points). Values for $T_{1\rho}(H_zC_zD_y)$ were measured using ^{2}H relaxation delays of 1, 2, 4, 6, 8, 10, 12, 16, 20, and 30 ms (10 time points). The time domain data were apodized with cosine-bell functions in both the ^{1}H and ^{13}C dimensions. The data were Fourier transformed into real (ReRe) frequency-domain matrixes having a final size of 512 × 512 points. In these final spectral matrixes, the ^{1}H dimension ranged from 3.13 to −1.67 ppm.

Sequential Resonance Assignment. Assignments for ^{15}N, ^1H_N, $^1H^{\alpha}$, $^1H^{\beta}$, $^{13}C^{\alpha}$, and $^{13}C^{\beta}$ resonances were obtained by semiautomated analyses (*40*, *41*) of two-dimensional (2D) ^{1}H−^{15}N HSQC and three-dimensional (3D) HNCACB, CBCA(CO)NH, HBHANH, and HBHA(CO)NH spectra. Methyl group ^{1}H and ^{13}C resonances were assigned from interactive analyses of 3D HCCH-TOCSY spectra. Acquisition and processing details for these 2D and 3D NMR experiments are contained in the Supporting Information.

NMR Relaxation Analysis. Relaxation parameters were evaluated on the basis of peak heights. To avoid underestimating the errors in the derived parameters, the standard deviations of the peak heights were set to twice the root-mean-square (rms) baseline noise observed in the corresponding spectra. The {^{1}H}−^{15}N steady-state NOE values were determined by evaluating the ratio of cross-peak heights from experiments recorded with and without ^{1}H saturation (NOE = I_{sat}/I_{unsat}). Error estimates for the NOE values were derived from standard error propagation. ^{15}N and ^{2}H relaxation rates were determined from a nonlinear least-squares fitting of the peak height data to exponential decays (*17*, *42*). The errors in the relaxation rates were estimated by generating simulated data sets from random Gaussian distributions of the peak intensities, with the mean of each distribution being set to the respective experimentally measured height.

The expressions relating ^{2}H and ^{15}N relaxation parameters to spectral density functions have been given elsewhere (*31*, *32*, *43*) and are described in the Supporting Information. Motional parameters can be derived from relaxation parameters using model-free spectral density functions (*22*−*25*). In this study, three functional forms were used to fit the ^{15}N relaxation data. In order of increasing complexity, these are as follows:

$$J(\omega) = S^2\tau_r/(1 + \omega^2\tau_r^2) \quad (1)$$

$$J(\omega) = S^2\tau_r/(1 + \omega^2\tau_r^2) + (1 - S^2)\tau/(1 + \omega^2\tau^2) \quad (2)$$

$$J(\omega) = S_f^2S_s^2\tau_r/(1 + \omega^2\tau_r^2) + S_f^2(1 - S_s^2)\tau_s'/(1 + \omega^2\tau_s'^2) \quad (3)$$

In these expressions, S^2 is the total generalized order parameter (which depends on the amplitudes of picosecond to nanosecond motions), τ_r is the overall molecular rotational correlation time, τ is an effective correlation time resulting from internal motions characterized by a single internal correlation time τ_e ($1/\tau = 1/\tau_e + 1/\tau_r$), S_f^2 and S_s^2 are order parameters corresponding to fast and slow internal picosecond to nanosecond motions with time scales differing by at least 1 order of magnitude, respectively (note, $S^2 = S_f^2S_s^2$), and τ_s' is an effective correlation time given by $1/\tau_s' = 1/\tau_s + 1/\tau_r$, where τ_s is the correlation time associated with slower internal motions. The τ_r value is treated as a global parameter determined by a preliminary global fitting of the data. Equations 1−3 contain, respectively, one, two, and three adjustable parameters. In addition, exchange contributions to $R_2(N)$, R_{2ex}, can be included in the analysis with eqs 1 and 2, resulting in fits that now involve, respectively, two and three residue-specific parameters.

The global τ_r was determined by a global fit that included all residues with $T_1(N)$ and $T_2(N)$ values within one standard deviation of the corresponding mean and with {^{1}H}−^{15}N NOE > 0.70. This global fit assumed $J(\omega)$ given by eq 2 for all included residues. After the global τ_r was determined, ^{15}N model-free parameters and error estimates were independently derived for each residue by numerical fits to their respective relaxation data. The fits were performed using a grid search followed by the Levenberg−Marquardt algorithm (*44*) to minimize χ^2 as described (*42*). The errors in the fitted model-free parameters of each residue were subsequently estimated by generating 100 simulated data sets of relaxation parameters from a Gaussian random distribution. The mean of the distribution was set to the calculated relaxation parameter, and the standard deviation was set to the estimated error of the relaxation parameter.

To select the model-free parameters to include in the fits of the ^{15}N relaxation data, we have adopted the following protocol, which is similar to the approaches described by

Palmer and co-workers (*21*) and Kay and co-workers (*19*). Initially, for all residues, the ^{15}N relaxation data are fit using eq 1 without a R_{2ex} term. This constitutes a one-parameter (S^2) fit. If, for a given residue, this simple model reproduces all of the ^{15}N relaxation data within their errors (within the 95% confidence interval defined by an *F* test), the analysis is concluded. If the ^{15}N relaxation data are not reproduced, then the two-parameter fits are performed: one with eq 2 (S^2 and τ_e) and one with eq 1 (S^2) and R_{2ex}. If either of these models reproduces all of the ^{15}N relaxation data within their errors, the analysis is concluded. If the ^{15}N relaxation data are not reproduced, then the three-parameter fits are performed: one with eq 3 (S_f^2, S_s^2, and τ_s) and one with eq 2 (S^2 and τ_e) and R_{2ex}; then the best fit is selected. In all cases, the model-free parameters are restricted to within physically reasonable ranges: $1 \geq S^2 \geq 0$, $\tau_e < \tau_r$, $\tau_s < \tau_r$, and $R_{2ex} \geq 0$. All of the fits were performed with a modified version of FELIX (Hare Research, Inc.; M. S. Friedrichs, unpublished). To check for consistency, the fits were repeated with the program j_f77, which was kindly provided by L. E. Kay and N. A. Farrow. If a fit to within the 95% confidence level could not be obtained using any model with either program, the best overall fit was selected as a tentative representation of the dynamic behavior. The ^{15}N relaxation data were also analyzed using the reduced spectral density mapping approach (*26*−*30*, *45*), as described in the Supporting Information.

The ^{2}H relaxation rates were fit assuming the global τ_r determined from the ^{15}N relaxation data, and further assuming that eq 2 holds for all methyl groups (*31*, *32*). Thus, for each methyl group, values for S^2 and τ_e are obtained. The order parameter for the methyl group symmetry axis vector, S^2_{axis}, is given by $S^2_{axis} = 9.009S^2$. S^2_{axis} is restricted to $1 \geq S^2_{axis} \geq 0$.

Structural Analysis and Modeling. High-resolution X-ray structures of human M-FABP (*5*) and murine A-LBP (*4*) are available. Since no structure of human apo-M-FABP is available, we have used the 1.4 Å resolution X-ray structure of human M-FABP complexed with stearate (PDB code 1HMT; *5*) for analysis purposes. The stearate was removed for accessible surface area calculations (see below), and only the major conformer was retained for those residues showing discrete conformations (V32, T36, T39, V80, T85, T102, L113, and T125). No major conformational changes are seen with different fatty acids bound to M-FABP (*5*); therefore, 1HMT should be a reasonably accurate model for the apoprotein as well.

A homology model of human apo-A-LBP was constructed starting from the 1.7 Å resolution X-ray structure of murine apo-A-LBP (PDB code 1LIB; *4*). The Look program (Molecular Applications Group, Palo Alto, CA) was used to construct the homology model. There are 11 residue substitutions upon going from murine to human A-LBP: L48 → V48, V49 → I49, R52 → K52, K65 → I65, V68 → Q68, I73 → V73, I83 → T83, A90 → V90, N93 → H93, D109 → E109, and G110 → D110. Most of these are surface substitutions; the only substitution near the binding cavity is the one at residue 93. The "model mutant" facility of Look was used to perform local conformational searchs (*46*, *47*) around the mutated residues while holding the remaining side chains and the polypeptide backbone fixed.

Hydrogen atoms were built onto the modeled M-FABP and A-LBP structures using the HBUILD routine of X-PLOR (*48*), and a 4° step size was used for the dihedral angle search if the hydrogen atom placement was not unique. In addition, all atoms for residues M0 and A132 were built onto the M-FABP structure using standard internal coordinates with X-PLOR. The accessible surface areas (*49*) of each residue (backbone and side chain) were computed with X-PLOR using a 1.4 Å probe radius.

RESULTS AND DISCUSSION

NMR Assignments and Slow Conformational Exchange. Both backbone and methyl side chain resonances in apo-A-LBP and apo-M-FABP were sequentially assigned by a general approach described previously (*40*, *41*). Henceforth, A-LBP and M-FABP refer to the apoprotein unless specified otherwise. Generalized spin systems, or residue information data structures (RIDS; *40*), were initially established on the basis of peaks observed in the 2D ^{15}N−^{1}H$_N$ HSQC spectra. This provided ^{15}N(*i*) and ^{1}H$_N$(*i*) chemical shift entries for each RID *i*. Data from the 3D triple-resonance spectra were subsequently loaded into RIDs in a semiautomated fashion (*41*). New RIDs were established as needed. At the end of this process, RIDs generally contained chemical shift entries for ^{15}N(*i*), ^{1}H$_N$(*i*), ^{1}H$^\alpha$(*i*), ^{1}H$^\alpha$(*i*−1), ^{1}H$^\beta$(*i*), ^{1}H$^\beta$(*i*−1), ^{13}C$^\alpha$(*i*), ^{13}C$^\alpha$(*i*−1), ^{13}C$^\beta$(*i*), and ^{13}C$^\beta$(*i*−1). The RIDs were then automatically linked and assigned (*40*). Methyl group ^{1}H and ^{13}C assignments were subsequently derived from the 3D HCCH-TOCSY spectra. Since our primary goal was to characterize the backbone dynamics and the dynamics of methyl-containing side chains, no effort has yet been made to obtain comprehensive side chain assignments.

Tables S1 and S2 of the Supporting Information contain the resonance assignments for A-LBP and M-FABP. Backbone ^{1}H$_N$ and ^{15}N assignments were obtained for 119 residues in A-LBP and for 125 residues in M-FABP. In A-LBP, ^{1}H$_N$ and ^{15}N assignments were not obtained for the following residues: N15, F27, A28, K37, E54, T56, A75, G88, R108, and D111. In M-FABP, ^{1}H$_N$ and ^{15}N assignments were not obtained for the following residues: N15, D17, F27, K37, T56, and G88. In all cases, the unassigned residues occur in relatively exposed regions. The ^{1}H$_N$ and ^{15}N resonances of these unassigned residues are missing from both the 2D ^{15}N−^{1}H HSQC and 3D triple-resonance spectra, indicating that the intensities of these resonances are attenuated by extreme line broadening and/or saturation transfer.

^{1}H$_N$ and ^{15}N resonances indicative of minor states (populations of ∼5 to ∼25%) have been assigned for some residues in both proteins (see Tables S1 and S2 of the Supporting Information). In A-LBP, minor states were observed for eight residues, all of which are within or spatially near the N-terminal segment (Figure 3A). Interestingly, F4 and V5 show three and two minor states, respectively. In M-FABP, 23 residues display minor ^{1}H$_N$ and ^{15}N resonances. Residues with minor ^{1}H$_N$ and ^{15}N resonances are distributed throughout the M-FABP structure (Figure 3B). As with A-LBP, human M-FABP displays minor states within and around the N-terminal segment. In addition, four residues in M-FABP display minor methyl group ^{1}H and ^{13}C resonances; these residues are V25, V32, T53, and L113.

Distinct resonances are observed for the minor states in both proteins, indicating that the lifetimes of these states must

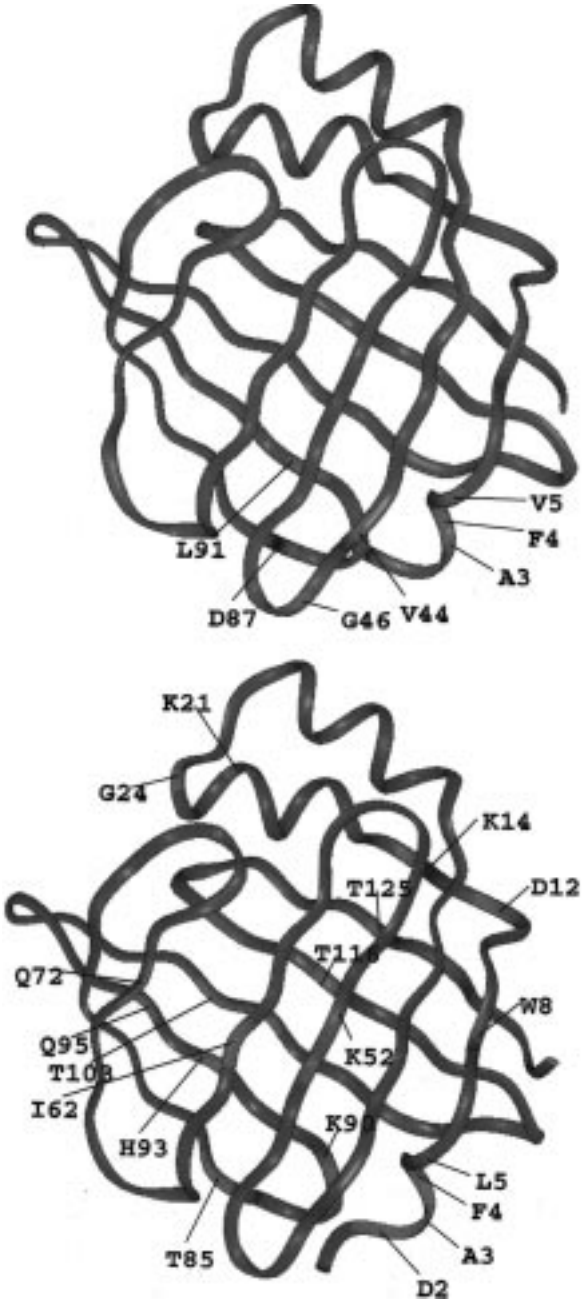

FIGURE 3: Residues with minor backbone ^{15}N and $^{1}H_N$ resonances mapped onto color-coded solid ribbon representations of the proteins. Residues for which minor ^{15}N and $^{1}H_N$ resonances have been assigned are shown in red; all other residues are shown in blue. Selected residues are labeled. (A, top) Minor states of A-LBP mapped onto the human A-LBP homology model, derived from PDB entry 1LIB. (B, bottom) Minor states of M-FABP mapped on to the M-FABP X-ray structure (1HMT). These images were created using InsightII (MSI, San Diego, CA).

be on the order of 100 ms or longer. These states may be due to either chemical or conformational heterogeneity. With regard to chemical heterogeneity, we have found no evidence of limited proteolysis using SDS−PAGE. N-Terminal sequencing indicated that the N-terminal methionine was fully intact in M-FABP and fully cleaved in A-LBP, and mass spectrometry revealed no evidence of N-terminal Met+/Met− heterogeneity. The minor states are likely to be long-lived minor conformational states. In general, the $^{1}H_N$ and ^{15}N resonances are the most affected, suggesting that many of the minor states may involve subtle differences in backbone hydrogen bonds. It is worth noting that minor states were observed for 25 residues in bovine M-FABP with bound palmitic acid (*50*). All of the relaxation data reported below reflect only the major state for those residues displaying both major and minor states. Major-state ^{1}H and ^{13}C assignments have been obtained for all methyl groups in both proteins.

Table 1: Average, Maximum, and Minimum ^{15}N and ^{2}H Relaxation Parameters for both Apo-A-LBP and Apo-M-FABP

	average	maximum	residue	minimum	residue
		T_1(N) (ms)			
A-LBP	630 ± 76	739 ± 21	V73	431 ± 20	F57
M-FABP	676 ± 81	830 ± 14	A132	341 ± 10	G46
		T_2(N) (ms)			
A-LBP	79.1 ± 11	97.0 ± 3.5	D87	40.9 ± 2.1	A33
M-FABP	77.9 ± 12	156.6 ± 2.9	A132	59.2 ± 2.1	F57
		$\{^{1}H\}-^{15}N$ NOE			
A-LBP				0.63 ± 0.03	K58-N59
M-FABP				0.23 ± 0.01	A132
		T_1(D) (ms)			
A-LBP	70.4 ± 43.9	248.3 ± 8.2	M35 ϵ	22.7 ± 4.6	V25 γ_1
M-FABP	68.3 ± 45.7	273.4 ± 8.7	M0 ϵ	26.7 ± 2.4	L5 δ_1
		$T_{1\rho}$(D) (ms)			
A-LBP	12.5 ± 8.0	54.9 ± 1.8	M35 ϵ	7.1 ± 0.4	V80 γ_1
M-FABP	13.9 ± 14.4	103.4 ± 5.5	M0 ϵ	6.3 ± 0.3	A122 β

^{15}N and ^{2}H Relaxation Parameters. Throughout the ensuing discussion, the standard deviation reported for the average value of a relaxation parameter is the standard deviation over all characterized sites, reflecting the distribution of that relaxation parameter. The standard deviation reported for a site-specific relaxation parameter is the error associated with that specific site. For both A-LBP and M-FABP, 111 peaks were sufficiently resolved and sufficiently intense in the $^{1}H-^{15}N$ correlation spectra to allow measurement of the ^{15}N relaxation parameters. Table 1 reports the average, maximum, and minimum T_1(N) and T_2(N) values for each protein over these 111 residues. The minimum $\{^{1}H\}-^{15}N$ NOE value is also reported for each protein over these 111 residues. T_1(N), T_2(N), and $\{^{1}H\}-^{15}N$ NOE values for each measured residue in both A-LBP and M-FABP are listed in Tables S3 and S4, respectively, of the Supporting Information.

Although all methyl group resonances have been assigned for both proteins, significant overlap and significant intensity variation exist for peaks in the 2D $^{1}H-^{13}C$ correlation spectra. In total, ^{2}H relaxation parameters could be measured for 42 out of 82 methyl groups in A-LBP and for 53 out of 90 methyl groups in M-FABP. The average, maximum, and minimum T_1(D) and $T_{1\rho}$(D) values are reported in Table 1 for each protein. T_1(D), $T_{1\rho}$(D), and $T_1(H_zC_z)$ values for each measured methyl group in both A-LBP and M-FABP are listed in Tables S5 and S6, respectively, of the Supporting Information. One special case did come to light during the analysis of the ^{2}H relaxation data. In A-LBP, the two methyl group resonances of L113 overlap completely; both δ-carbons resonate at 25.1 ppm, and all δ-protons resonate at −0.12 ppm. Because the $T_1(H_zC_zD_z)$, $T_1(H_zC_z)$, and $T_{1\rho}(H_zC_zD_y)$ data for these two methyl groups could be fit as single-exponential decays, both methyl groups were assumed to have identical relaxation properties.

Model-Free Analysis of ^{15}N Relaxation Data. The first task in extracting motional information from ^{15}N relaxation

data involves determining the parameters that define the overall rotational motion of the protein. Isotropic motion is defined by the single parameter τ_r. Principle moments of the inertial tensors, computed from the A-LBP and M-FABP structures, yield ratios of 1.00:1.19:1.42 and 1.00:1.21:1.46, respectively. These ratios indicate that the assumption of isotropic motion is reasonable for both proteins, with the following caveats taken into consideration. Model-free spectral density functions that take into account overall rotational anisotropy are available (*22*, *23*). In general, for proteins that are moderately asymmetric, the S^2 values obtained are insenstive to the choice of an isotropic versus an anisotropic motional model (*51*−*53*). Neglect of anistropy for moderately asymmetric proteins can lead to moderate ($\sim$1.0 s^{-1} or less) overestimates of R_{2ex} values (*53*−*55*). Therefore, R_{2ex} values of $<$1.0 s^{-1} must be viewed with caution when isotropic motion is assumed. Neglect of anisotropy may also lead to a distortion of the internal correlation time when the extended model-free formalism (eq 3) is required for an adequate fit (*54*, *56*). For these reasons, we focus primarily on S^2 values and on R_{2ex} values of $\geq$2.0 s^{-1}; we do not discuss in detail internal correlation times or residues with R_{2ex} values of $<$2.0 s^{-1}. It should be pointed out that using an anisotropic model has its own set of disadvantages, requiring one either to use N−H vector orientations derived from a structural model (*57*−*60*) or to fix internal correlation times during the fitting process (*61*, *62*). Also, if one does not use N−H vector orientations from a structural model, the simplest possible anisotropic model contains four adjustable parameters, whereas the simplest isotropic model (see model 1 below) contains only two adjustable parameters. Clearly, an anisotropic model is essential in cases of highly asymmetric or multidomain proteins (*51*, *59*, *60*, *62*). For the moderately asymmetric proteins examined in this study, we choose to employ the more widely used isotropic analysis, focusing on those parameters that are expected to be insensitive to the choice of global motional model.

Assuming isotropic motion, an estimate of τ_r can be derived from T_1(N)/T_2(N) ratios that fall within one standard deviation of the mean T_1(N)/T_2(N) ratio (*14*). This approach assumes that $J(\omega)$ can be represented by eq 1 for residues satisfying the T_1(N)/T_2(N) criteria. Under such an assumption, T_1(N)/T_2(N) depends only on τ_r.

We have adopted an alternate approach to obtain τ_r (*42*). A global fit of the ^{15}N T_1, T_2, and NOE data is performed for selected residues assuming that $J(\omega)$ can be represented by eq 2. Subsequently, $2N + 1$ model-free parameters (τ_e and S^2 for N selected residues and τ_r) are fit to $3N$ relaxation parameters (^{15}N T_1, T_2, and NOE values for N selected residues) to obtain τ_r. Moreover, this global analysis was used only to obtain a value for τ_r; residue-specific parameters obtained from this global analysis were not considered further.

Residues selected for the global τ_r fitting had to have the following ^{15}N relaxation characteristics: a T_1(N) within one standard deviation of the mean, a T_2(N) within one standard deviation of the mean, and a {^{1}H}−^{15}N NOE of $>$0.70. In A-LBP, 53 residues satisfied these "rigid residue" criteria. Using those 53 residues, the τ_r for A-LBP was estimated to be 8.70 $\pm$ 0.10 ns/rad. In M-FABP, 83 residues satisfied these rigid residue criteria. Using those 83 residues, the τ_r for M-FABP was estimated to be 9.05 $\pm$ 0.10 ns/rad. It should be noted that uncertainties associated with τ_r values will primarily affect the absolute S^2 values; the relative S^2 values for a given protein are maintained even with errors in τ_r that are quite large (*63*). Since the τ_r values obtained for A-LBP and M-FABP are both close in absolute terms and consistent with M-FABP having two more residues than A-LBP, a comparison of the S^2 values obtained for both proteins is expected to be meaningful. With the τ_r values determined for both proteins, the ^{15}N relaxation data were subsequently fit on an individual residue basis for each characterized residue (see Experimental Procedures). Five models of $J(\omega)$ were possible: eq 1 without R_{2ex} (model 1), eq 2 without R_{2ex} (model 2), eq 1 with R_{2ex} (model 3), eq 3 without R_{2ex} (model 4), and eq 2 with R_{2ex} (model 5).

Table S7 of the Supporting Information lists in detail the results of the ^{15}N model-free analysis on A-LBP. Figure 4 depicts backbone HN S^2 values, R_{2ex} values, and backbone atom solvent-accessible surface areas for this protein. In summary, for A-LBP, 42 residues were fit by model 1, 10 residues were fit by model 2, 22 residues were fit by model 3, 13 residues were fit by model 4, and 23 residues were fit by model 5. The data for D98 yielded extremely poor fits with all models (the best $\chi^2 = 88.43$ using model 3); therefore, no model-free parameters are reported for this residue. The potential reasons for such poor fitting are discussed below in the context of the reduced spectral density mapping. A-LBP has 23 residues with S^2 values of $\leq$0.70 and 32 residues with R_{2ex} values of $\geq$2.0 s^{-1}. Interestingly, 13 residues have both an S^2 value of $\leq$0.70 and an R_{2ex} value of $\geq$2.0 s^{-1}, indicative of significant motions on multiple time scales. Of the 46 A-LBP residues requiring models 2, 4, or 5 for an adequate fit, 42 yielded internal correlation times (τ_e or τ_s) of $>$1.0 ns (Supporting Information), suggestive of motions on the nanosecond time scale. In general, internal correlation times are defined quite imprecisely by the ^{15}N relaxation data, and therefore are not discussed here in detail. It is worth noting that 28 residues in apo-I-FABP yielded internal correlation times of $>$1.0 ns (*6*).

Table S8 of the Supporting Information lists the ^{15}N model-free parameters for M-FABP; Figure 5 shows the backbone S^2 values, R_{2ex} values, and backbone atom solvent-accessible surface areas. For M-FABP, 49 residues were fit by model 1, 7 residues were fit by model 2, 26 residues were fit by model 3, 5 residues were fit by model 4, and 24 residues were fit by model 5. A poor fit was obtained for G46 ($\chi^2 = 31.82$ using model 2), so the model-free parameters reported for this residue must be regarded as approximations. M-FABP has 12 residues with S^2 values of $\leq$0.70 and 14 residues with R_{2ex} values of $\geq$2.0 s^{-1}. Eight residues have both an S^2 value of $\leq$0.70 and an R_{2ex} value of $\geq$2.0 s^{-1}, and 28 residues have internal correlation times of $>$1.0 ns (Supporting Information). Overall, these results demonstrate that substantially fewer residues in M-FABP, relative to A-LBP, display significant dynamics on the picosecond to nanosecond and/or microsecond to millisecond time scales.

Reduced Spectral Density Mapping of ^{15}N Relaxation Data. Reduced spectral density values for A-LBP and M-FABP are listed in Tables S9 and S10 of the Supporting Information. For A-LBP, the average values of $J_{eff}(0)$, $J(\omega_N)$,

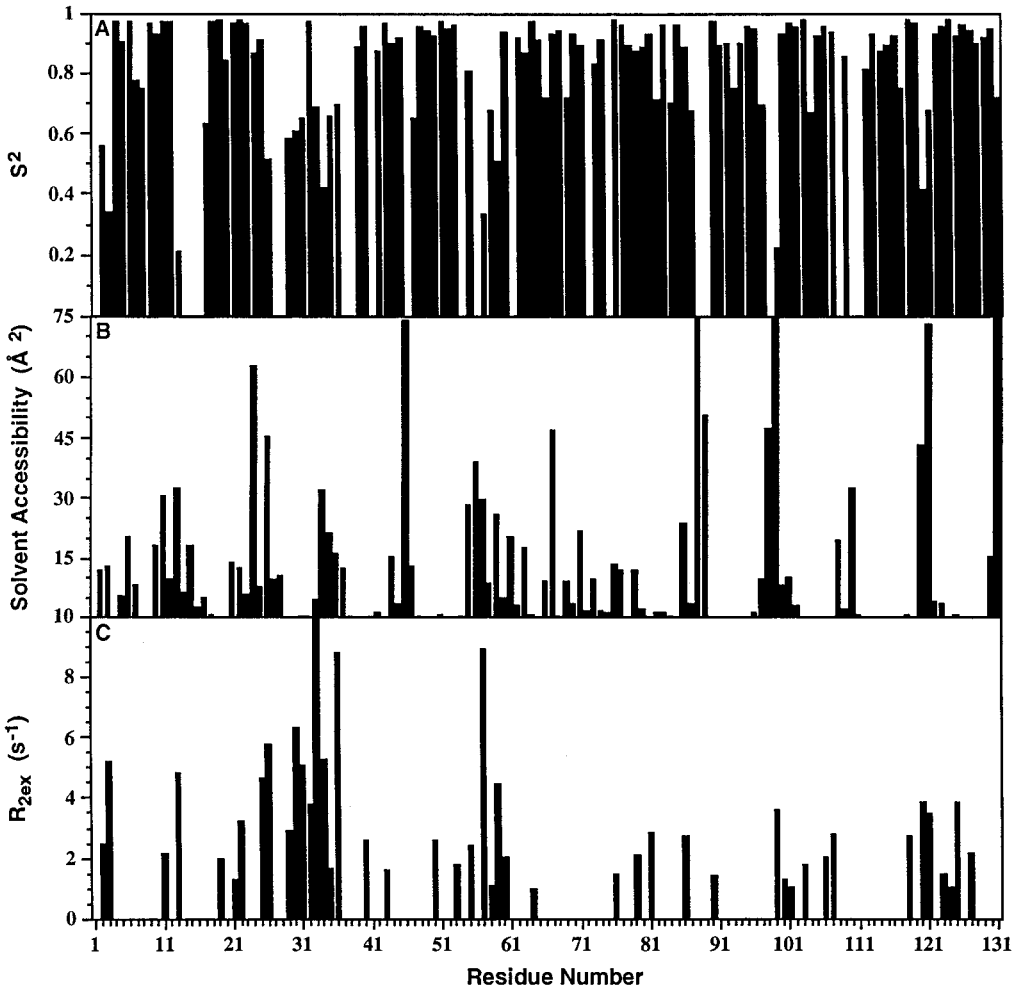

FIGURE 4: Histograms summarizing the ^{15}N model-free parameters and solvent-accessible surface areas for A-LBP. (A) Backbone amide S^2 values. (B) Backbone atom solvent-accessible surface areas (Å^2). (C) Backbone amide R_{2ex} values (s^{-1}). The value for A33 (14.2 s^{-1}) is off the scale.

and $J_{ave}(\omega_H)$ are 8.81 ± 1.48 ns/rad, 0.762 ± 0.107 ns/rad, and 12.6 ± 4.5 ps/rad, respectively, while for M-FABP, these values are 8.95 ± 1.10 ns/rad, 0.711 ± 0.107 ns/rad, and 12.3 ± 7.6 ps/rad, respectively.

In general, the spectral density $J(\omega)$ reflects the power available from magnetic field fluctuations at the transition frequency ω. For a protein undergoing isotropic overall motion, an interatomic vector that is completely rigid in the molecular frame will yield a $J_{eff}(0)$ equal to τ_r. Highly restricted vectors will also have relatively high values of $J(\omega_N)$ and relatively low values of $J_{ave}(\omega_H)$. Vectors with significant picosecond to nanosecond time scale motions will have low values of $J_{eff}(0)$ and $J(\omega_N)$ and high values of $J_{ave}(\omega)$. Significant R_{2ex} values will increase $J_{eff}(0)$ beyond τ_r for a vector that is rigid on the picosecond to nanosecond time scale. As discussed below, deviations from these simple patterns may be indicative of significant motions on multiple time scales.

On the basis of the model-free analysis, many A-LBP and M-FABP residues appear to be quite mobile on both the picosecond to nanosecond and microsecond to millisecond time scales. A number of these same residues also display deviations from the simple patterns of reduced spectral densities described above. For example, many A-LBP residues in or near α-helix II (residues 28−35) have small S^2 and large R_{2ex} values; many of these same residues display above average values for all three reduced spectral density functions. A33 of A-LBP has above average values for all three reduced spectral density funtions, including an extremely high $J_{eff}(0)$ value (17.07 ± 0.92 ns/rad), consistent with its massive R_{2ex} value (14.2 ± 1.2 s^{-1}). These results lend confidence to the model-free analysis for these residues; i.e., both approaches indicate significant motions on both the picosecond to nanosecond and microsecond millisecond time scales.

Residues that could not be fit well by the model-free approach also do not yield simple patterns of reduced spectral density values. For example, D98 of A-LBP yields high values for all three spectral density functions, while G46 of M-FABP yields a very low value for $J_{eff}(0)$ and high values for $J(\omega_N)$ and $J_{ave}(\omega_H)$. For these two residues, the reduced spectral density functions indicate that the poor model-free fits are due to dynamic complexity, rather than to poor performance of the model-free fitting routines.

One precaution must be noted when interpreting reduced spectral density functions: for residues experiencing significant motions on multiple time scales, the opposing effects of picosecond to nanosecond and microsecond to millisecond motions on $J_{eff}(0)$ can mask important aspects of the dynamic behavior. Consider T29 of A-LBP, for which $S^2 = 0.59 \pm 0.08$ and $R_{2ex} = 2.9 \pm 0.5$ s^{-1}. This residue yields $J_{eff}(0) = 8.60 \pm 0.24$ ns/rad, $J(\omega_N) = 0.934 \pm 0.031$ ns/rad, and

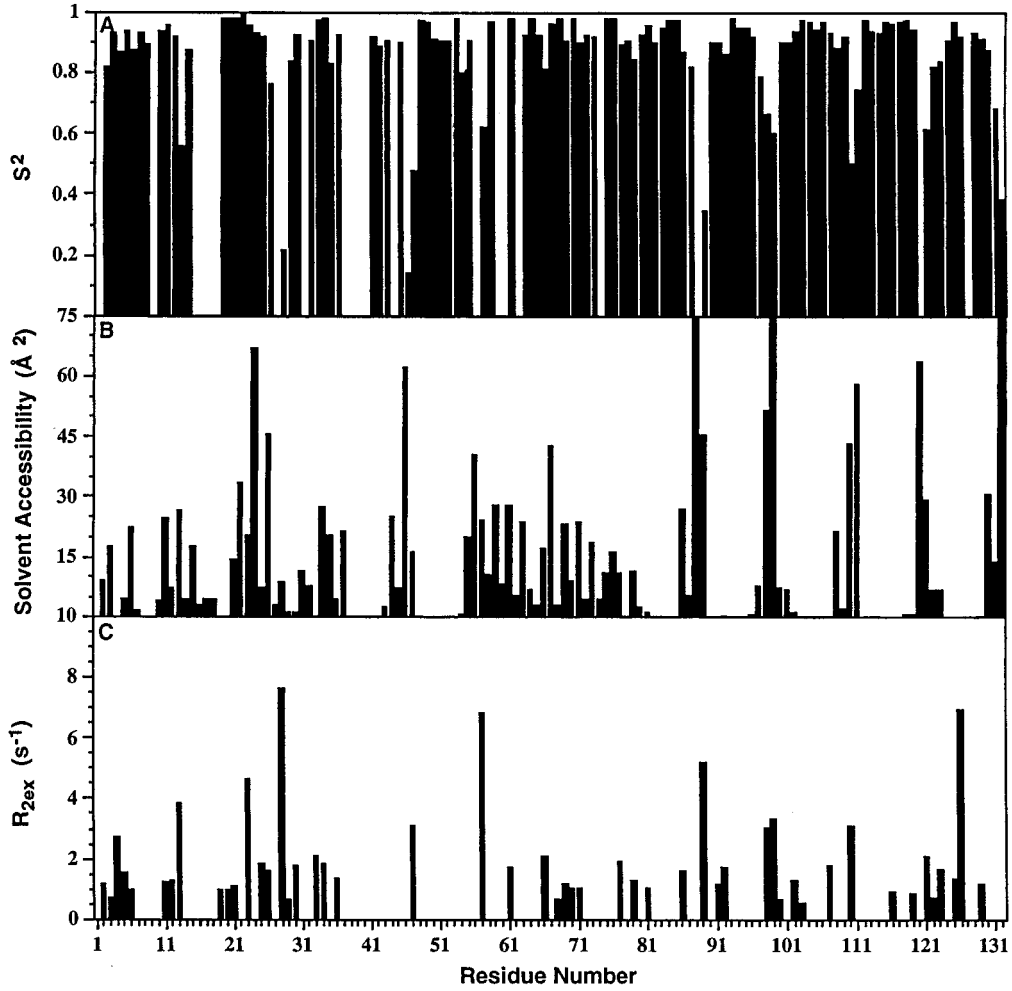

FIGURE 5: Histograms summarizing the ^{15}N model-free parameters and solvent-accessible surface areas for M-FABP. (A) Backbone amide S^2 values. (B) Backbone atom solvent-accessible surface areas (Å^2). (C) Backbone amide R_{2ex} values (s^{-1}).

$J_{ave}(\omega_H) = 17.3 \pm 3.7$ ps/rad. While the high value of $J_{ave}(\omega_H)$ indicates significant picosecond to nanosecond time scale motions, the microsecond to millisecond motions are not evident in the value of $J_{eff}(0)$. Since the vast majority of A-LBP and M-FABP residues were adequately fit by the model-free approach, the remainder of this article will focus on the results obtained using the model-free analysis.

A-LBP and M-FABP Backbone Dynamics. Panels A and B of Figure 6 display the $^1H-^{15}N$ S^2 values mapped onto the respective backbones of A-LBP and M-FABP. Highly rigid residues are colored blue, and highly flexible residues are colored red (see the Figure 6 legend for additional details). Specific regions in A-LBP display considerably greater flexibility on the picosecond to nanosecond time scale relative to those of M-FABP. In particular, many residues are significantly more flexible in A-LBP in the proposed ligand entry portal (*64*, *65*), which is in the vicinity of α-helix II and the C−D turn. For A-LBP and M-FABP, ^{15}N relaxation parameters have been obtained for eight corresponding residues between positions 26 and 36 (inclusive). For these residues, the average S^2 value is 0.64 ± 0.15 for A-LBP and 0.89 ± 0.07 for M-FABP. The A-LBP and M-FABP sequences differ at positions 31 and 34 in α-helix II (Figure 1). In particular, the glycine at position 34 in A-LBP may destabilize α-helix II. In the C−D turn, F57 and K58 have respective S^2 values of 0.33 ± 0.12 and 0.67 ± 0.04 in A-LBP, whereas these residues have respective S^2 values of 0.62 ± 0.08 and 0.96 ± 0.02 in M-FABP. Furthermore, I104 in β-strand I and C117 in β-strand J of A-LBP display lower S^2 values than the corresponding residues L104 and L117 in M-FABP. Residues 104 and 117 are important binding pocket residues.

The backbone S^2 results described above can be compared to results previously reported for apo-I-FABP (*6*). In the portal region of apo-I-FABP, the following residues exhibit S^2 values near 0: G31−D34 of α-helix II, N54 and F55 of the C−D turn, and A73, D74, and G75 of the E−F turn. In contrast, no evidence of high mobility in the E−F turn has been found for either A-LBP or M-FABP. Therefore, apo-I-FABP appears to be significantly more flexible on the picosecond to nanosecond time scale in the portal region than A-LBP; A-LBP is in turn significantly more flexible in this region than M-FABP. In contrast to these solution-state results, the 1.2 Å resolution crystal structure of apo-I-FABP (*66*) exhibits low temperature factors in both α-helix II and the C−D turn, whereas the 1.7 Å resolution crystal structure of murine A-LBP (*4*) exhibits high temperature factors in these regions. Thus, the profile of crystalline-state dynamics−disorder may in some cases differ significantly from that of solution-state dynamics.

Panels A and B of Figure 7 display the R_{2ex} values mapped onto the respective backbones of A-LBP and M-FABP. As with the picosecond to nanosecond time scale motions, A-LBP appears to be significantly more mobile than M-

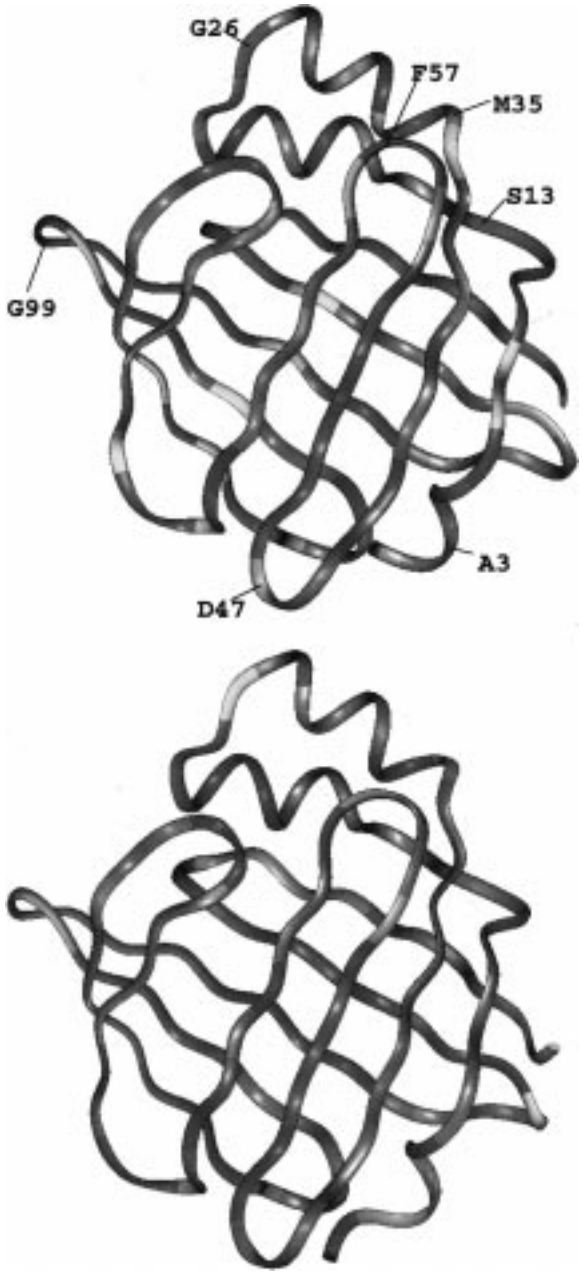

FIGURE 6: Backbone amide S^2 values mapped onto color-coded solid ribbon representations of the proteins. Gray indicates residues for which ^{15}N relaxation data are not available. The remaining residues are color-coded as follows. Residues with S^2 values of <0.50 are colored red. For the remaining characterized residues, the color is scaled from red ($S^2 = 0.50$) to yellow ($S^2 = 0.75$) to blue ($S^2 = 1.00$). (A, top) S^2 values for A-LBP mapped onto the human A-LBP homology model, derived from PDB entry 1LIB. Selected residues are labeled. (B, bottom) S^2 values for M-FABP mapped onto the M-FABP X-ray structure (1HMT). These images were created using InsightII.

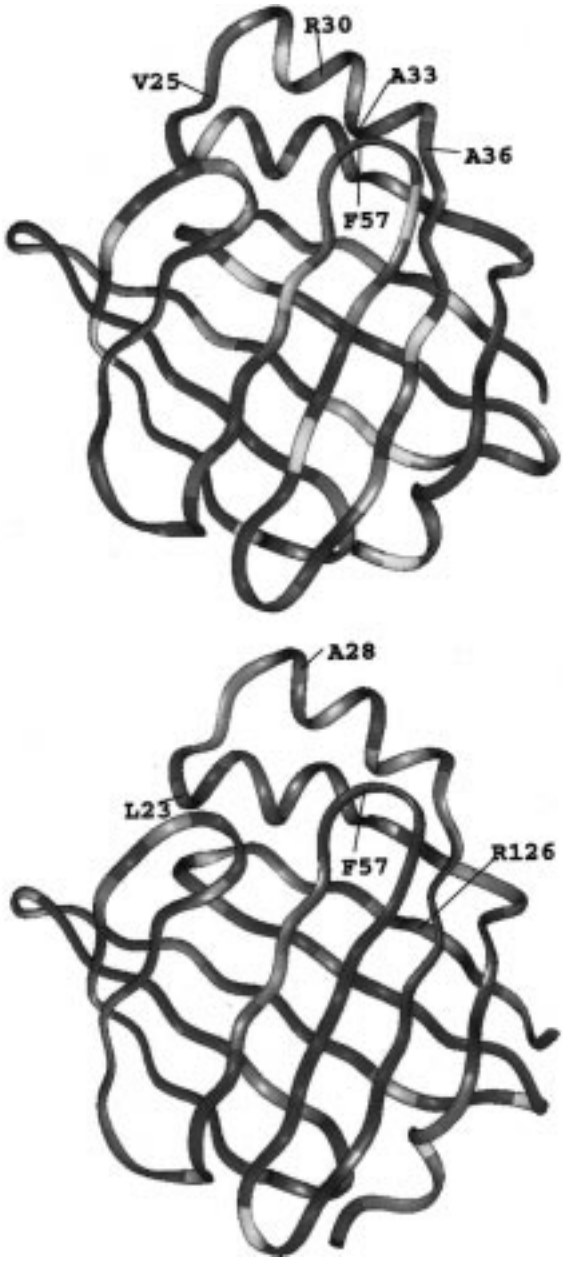

FIGURE 7: Backbone amide R_{2ex} values mapped onto color-coded solid ribbon representations of the proteins. Gray indicates residues for which ^{15}N relaxation data are not available. The remaining residues are color-coded as follows. Residues with R_{2ex} values of >5.0 s^{-1} are colored red. For the remaining characterized residues, the color is scaled from red ($R_{2ex} = 5.0$ s^{-1}) to yellow ($R_{2ex} = 2.5$ s^{-1}) to blue ($R_{2ex} = 0.0$ s^{-1}). (A, top) R_{2ex} values for A-LBP mapped on to the human A-LBP homology model, derived from PDB entry 1LIB. Selected residues are labeled. (B, bottom) R_{2ex} values for apo-M-FABP mapped on to the M-FABP X-ray structure (1HMT). Selected residues are labeled. These images were created using InsightII.

FABP on the microsecond to millisecond time scale, especially in the portal region. Significant R_{2ex} values were also obtained for many of the residues in the portal region of I-FABP (*6*).

To examine the dynamics of the portal region in more detail, we will focus on two residues in particular: A33 and F57. In A-LBP, these residues have respective R_{2ex} values of 14.2 ± 1.2 and 8.9 ± 1.2 s^{-1}, while in M-FABP, the respective R_{2ex} values are 2.1 ± 0.6 and 6.8 ± 0.9 s^{-1}. The value obtained for A33 in A-LBP is unusually large. While it is not possible to rigorously identify the underlying cause of such a large R_{2ex} value using the data currently available, we nevertheless can put forth a reasonable hypothesis that may be testable in future studies. Before this hypothesis is described in detail, it is necessary to discuss the general nature of exchange contributions to R_2. Unlike S^2 values, which are directly related to motional amplitudes (*22*, *23*, *42*, *67*), the relationship between R_{2ex} values and motional amplitudes is indirect. Any process that produces a variation in the ^{15}N chemical shift at the appropriate rate will produce

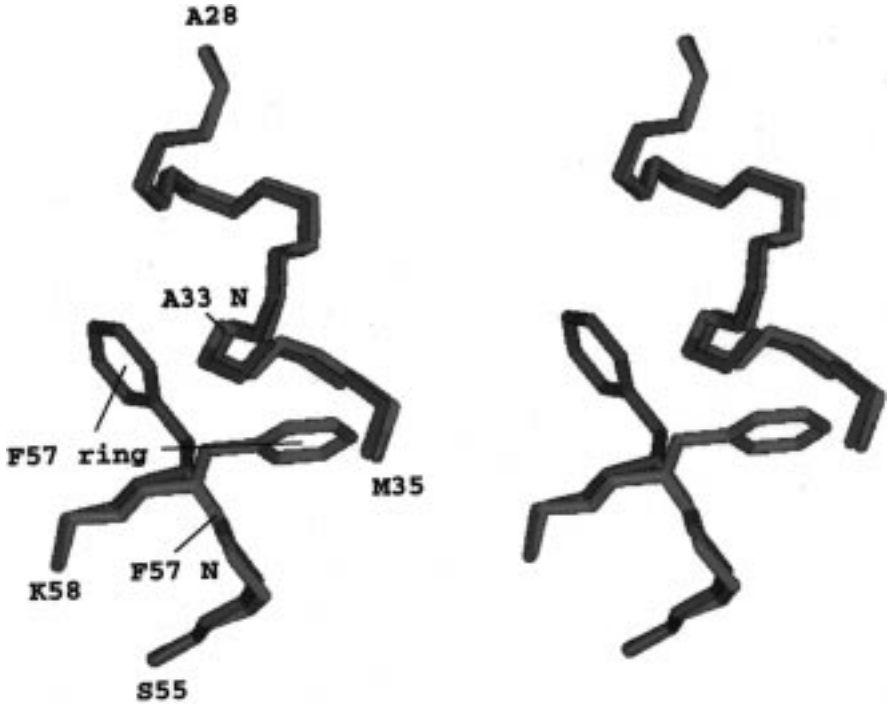

FIGURE 8: Stereoview showing the alternate conformations observed for F57 in murine A-LBP in the apo and stearate-bound states (*4*). The backbone N, C^{α}, and C traces of residues 28−35 and residues 55−58 are shown. The apo form (1LIB) is colored green, and the stearate-bound form (1LIF) is colored red. The N atoms of A33 and F57 are colored blue for both forms. This image was created using InsightII.

an exchange contribution. For a two-state exchange process, the value of R_{2ex} depends on the square of the chemical shift difference between the states, the rate of the exchange process, and the product of the fractional populations of the states (*68*−*70*).

Given this background, we can suggest a possible cause for the large R_{2ex} values found for A33 and F57 in A-LBP. Xu et al. (*4*) reported significantly different conformations for the F57 side chain in the apo and fatty acid-bound forms of murine A-LBP. Bound fatty acids positioned F57 in an "open" conformation, extending away from the body of the protein, whereas F57 was found in a "closed" conformation in the apoprotein. If static, this closed conformation would preclude ligands from entering the portal. Examples of these two conformational states are shown in Figure 8. Xu et al. (*4*) speculated that F57 must be able to transiently swing into the open state to allow ligand entry. We suggest that the large R_{2ex} values found for A33 and F57 in A-LBP provide direct evidence for a dynamic equilibrium between the open and closed states of F57. As can be seen in Figure 8, such a conformational change would be likely to perturb the chemical shifts of the A33 and F57 ^{15}N nuclei, as well as those of other residues in the portal region. We have previously suggested that reorientations of nearby aromatic rings, rather than motions of the $^{15}N-^{1}H$ vectors per se, are often the cause of observed R_2 exchange contributions (*17*). In the case of M-FABP, F57 still has a large R_{2ex}, but most of the remaining residues in the portal region show significantly smaller R_{2ex} values. This could be due to a number of factors (*68*−*70*); clearly, the nature of the microsecond to millisecond dynamics in the portal regions differs somewhat between A-LBP and M-FABP. If our hypothesis is correct, we expect that replacing F57 in A-LBP with a nonaromatic residue would result in a significantly smaller R_{2ex} value for A33.

We have also examined the data for possible relations between backbone atom solvent accessibilities and backbone dynamics. In a study of the backbone and side chain dynamics of hen egg white lysozyme (*20*), the authors reported that "the most significant correlations are found between residues with low order parameters and high surface accessibility in both crystal and solution structures." In contrast, A-LBP and M-FABP have yielded no clear correlation between backbone atom solvent accessibilities and backbone amide order parameters. For example, G24, which is highly exposed in both A-LBP and M-FABP with respective solvent accessibilities of 62.6 and 67.0 $Å^2$, is highly ordered in both proteins, with respective S^2 values of 0.87 ± 0.04 and 0.93 ± 0.03. However, the backbone atoms of residues 29−33 (part of α-helix II) in A-LBP exhibit both low accessibilities and relatively low S^2 values. In general, we conclude that local solvent accessibility, as determined from a "static" structure, is only one of many factors influencing the backbone dynamics of a specific residue. As such, local solvent accessibility alone is a poor predictor of local backbone dynamics.

The proposed iLBP ligand entry portal (*64*, *65*) can display highly varied backbone picosecond to nanosecond time scale dynamic behavior among iLBPs, progressing from relatively rigid in M-FAPB, to flexible in A-LBP, and finally to almost completely disordered in apo-I-FABP (*6*). In this context, a recent protein engineering study merits discussion. A helix-less variant of I-FABP has recently been shown to have a model-dependent pseudo-first-order association rate constant (k_2) for oleate similar to that for wild-type I-FABP, whereas the oleate dissociation rate was significantly slower for the wild-type protein (*71*). For the wild-type protein, the experimentally observed oleate association rate (k_{obs}) reached a limiting value of $\sim 1000\ s^{-1}$. The simplest binding model that fits all of the data included an equilibrium

between open and closed conformations of the helical region, with ligands binding to only the open state. It was concluded that the helical region regulates ligand affinity by altering the dissociation rate. These results suggest that the open conformation of the helix−loop−helix motif of I-FABP does not present a significant kinetic barrier to ligand entry. That this conclusion may apply only to I-FABP is suggested by the relatively more ordered ligand entry portals observed for both A-LBP and, especially, M-FABP. Assuming that the open states among the iLBPs are similar in terms of their average conformations, the more ordered ligand entry portals in A-LBP and M-FABP may result in more restrictive barriers to ligand entry in the open state. Consistent with this suggestion, Richieri et al. (*3*) reported larger association rate constants for I-FABP, relative to those of A-LBP and M-FABP, for all five different fatty acids that they examined. Thus, in addition to the slower open−closed interconversion, ligand association may be further influenced by the picosecond to nanosecond time scale mobility of the helical region.

Given the results described above, variations in the dynamics of the portal region may play an important role in ligand selectivity. In particular, because the protein backbone of A-LBP may be able to adopt a greater variety of conformations than that of M-FABP in response to different ligands, larger ligands may enter the A-LBP binding pocket more easily. Similar suggestions have recently been made regarding both ileal lipid-binding protein and the type III domains from fibronectin and tenascin. On the basis of relatively rapid hydrogen exchange rates, the wide ligand-binding specificity of ileal lipid-binding protein was suggested to be due in part to a weaker hydrogen bonding network in the β-sheets (*7*). This suggestion is consistent with the T4 lysozyme studies (*9*); i.e., a weaker hydrogen bonding network presumably enhances the binding pocket plasticity. Thus, although the long time scale processes involved in hydrogen exchange are unlikely to be directly involved in ligand binding, rapid exchange rates may provide a measure of local structural softness (*9*, *17*). In a different study (*72*), ^{15}N relaxation measurements have demonstrated that the RGD motif of the tenth fibronectin type III domain is much more flexible than the RGD motif of the third type III domain of tenascin. This result may possibly explain the broader binding specificity of the fibronectin type III domain (*72*).

Model-Free Analysis of ^{2}H Relaxation Data. The ^{2}H relaxation data were analyzed with $J(\omega)$ modeled exclusively by eq 2 (*31*, *32*). This analysis requires knowledge of a global τ_r value. A global τ_r value cannot be reliably determined from T_1(D)/$T_{1\rho}$(D) ratios because methyl groups generally display a wide range of dynamic behavior (*31*, *32*, *73*−*75*). Therefore, the global τ_r value used in the ^{2}H relaxation analysis was that determined from the model-free analysis of the ^{15}N relaxation data. This choice for the τ_r value was deemed reasonable because the sample temperatures, concentrations, and buffers were closely matched in both the ^{15}N and ^{2}H relaxation data sets. It is especially critical that both ^{15}N and ^{2}H relaxation experiments be performed in buffers with the same D_2O:H_2O ratio. D_2O is significantly more viscous than H_2O, resulting in a longer overall rotational correlation time in D_2O solutions (*76*).

Table 2: ^{2}H Model-Free Parameters, Accessible Surface Areas, and *B*-Factors for A-LBP

methyl	S^2_{axis}	τ_e (ps)	accessibility (Å^2)[a]	*B*-factor (Å^2)[b]
A3 β	0.78 ± 0.08	66.4 ± 6.3	13.2, 30.0	14.8
L10 δ_2	0.64 ± 0.05	26.0 ± 3.9	18.2, 5.9	12.3
V11 γ_2	0.38 ± 0.02	71.0 ± 2.1	30.7, 46.4	18.9
M20 ϵ	0.43 ± 0.02	17.9 ± 1.0	0.0, 8.6	22.2
V23 γ_1	0.66 ± 0.05	89.8 ± 6.0	5.9, 8.0	19.6
V23 γ_2	0.75 ± 0.05	39.6 ± 3.4	5.9, 8.0	19.6
V25 γ_1	0.71 ± 0.17	109.5 ± 26.8	8.0, 1.8	18.3
A28 β	0.75 ± 0.06	52.5 ± 4.0	10.6, 62.3	26.3
T29 γ_2	0.78 ± 0.06	40.6 ± 5.4	0.0, 34.9	24.0
M35 ϵ	0.11 ± 0.01	8.3 ± 0.4	21.5, 138.2	ND[c]
A36 β	0.96 ± 0.09	32.6 ± 4.7	16.2, 1.7	36.5
M40 ϵ	0.30 ± 0.01	12.6 ± 0.7	0.0, 2.6	26.5
I41 δ_1	0.30 ± 0.01	15.0 ± 0.7	0.5, 44.9	18.1
I41 γ_2	0.81 ± 0.04	36.7 ± 2.8	0.5, 44.9	16.8
I42 δ_1	0.75 ± 0.03	17.7 ± 2.0	1.3, 0.0	14.5
I42 γ_2	0.87 ± 0.04	24.4 ± 2.0	1.3, 0.0	9.0
V44 γ_2	0.37 ± 0.02	60.6 ± 2.1	15.1, 36.5	14.4
V48 γ_2	0.88 ± 0.04	51.0 ± 3.2	0.3, 54.7	−
I49 δ_1	0.31 ± 0.01	20.6 ± 1.2	0.0, 1.2	−
I51 δ_1	0.78 ± 0.04	14.0 ± 1.6	0.7, 0.7	10.7
I51 γ_2	0.95 ± 0.05	10.8 ± 1.8	0.7, 0.7	10.8
T56 γ_2	0.58 ± 0.03	48.8 ± 3.0	39.2, 107.4	31.0
I62 δ_1	0.79 ± 0.04	13.9 ± 1.7	3.3, 17.5	14.0
I62 γ_2	0.82 ± 0.05	34.6 ± 3.3	3.3, 17.5	12.7
I65 δ_1	0.45 ± 0.01	18.4 ± 0.9	0.0, 73.6	−
I65 γ_2	0.70 ± 0.03	60.8 ± 2.9	0.0, 73.6	−
A75 β	0.86 ± 0.09	50.0 ± 6.1	1.5, 33.0	17.7
V80 γ_1	0.90 ± 0.07	73.7 ± 6.3	2.3, 1.3	11.8
V80 γ_2	0.95 ± 0.06	17.1 ± 2.8	2.3, 1.3	11.8
I84 δ_1	0.75 ± 0.05	32.6 ± 3.1	0.3, 1.2	11.6
I84 γ_2	0.80 ± 0.06	61.5 ± 5.3	0.3, 1.2	8.3
L86 δ_1	0.37 ± 0.04	47.0 ± 4.4	23.8, 51.0	15.8
L86 δ_2	0.36 ± 0.02	63.3 ± 3.2	23.8, 51.0	15.8
V90 γ_1	0.78 ± 0.02	31.9 ± 1.6	0.0, 17.5	−
L91 δ_1	0.42 ± 0.02	51.9 ± 3.0	0.0, 0.0	11.6
L91 δ_2	0.33 ± 0.05	84.0 ± 8.6	0.0, 0.0	11.6
T103 γ_2	0.75 ± 0.06	54.0 ± 4.9	0.1, 46.0	15.8
I104 δ_1	0.39 ± 0.02	12.0 ± 0.9	0.0, 16.4	15.0
I104 γ_2	0.86 ± 0.05	28.0 ± 4.0	0.0, 16.4	16.9
L113 δ	0.18 ± 0.01	46.0 ± 1.5	0.0, 0.0	17.6
M119 ϵ	0.68 ± 0.01	6.1 ± 0.7	0.0, 8.7	19.3
A131 β	0.47 ± 0.02	37.9 ± 1.2	77.8, 18.7	15.0

[a] The first number is the accessible surface area for all backbone atoms, and the second number is the accessible surface area for all side chain atoms. These values were computed after modeling human A-LBP on the basis of the murine A-LBP structure (PDB entry 1LIB) and adding hydrogens. [b] Temperature factors for the methyl carbon as given in PDB entry 1LIB. For V and L residues, the methyl carbon *B*-factors were averaged. *B*-factor values are not given for residues that are not conserved between human and murine A-LBP. [c] ND, not determined.

Tables 2 and 3 report the results from the respective model-free analyses of the A-LBP and M-FABP ^{2}H relaxation data. The χ^2 values are negligible for all fits of the ^{2}H relaxation data. The resulting τ_e values are also generally well-defined. Tables 2 and 3 also list both the methyl carbon temperature factors (*B*-factors) and the backbone and side chain solvent-accessible areas for the characterized residues. In A-LBP, S^2_{axis} values range from 0.11 ± 0.01 (M35 ϵ-methyl) to 0.96 ± 0.09 (A36 β-methyl) and τ_e values range from 6.1 ± 0.7 ps (M119 ϵ-methyl) to 109.5 ± 26.8 ps (V25 γ_1-methyl). In M-FABP, S^2_{axis} values range from 0.05 ± 0.01 (M0 ϵ-methyl) to 0.99 ± 0.04 (V84 γ_2-methyl) and τ_e values range from 7.7 ± 2.7 ps (M20 ϵ-methyl) to 90.9 ± 10.5 ps (L5 δ_1-methyl).

Table 3: ^{2}H Model-Free Parameters, Accessible Surface Areas, and *B*-Factors for M-FABP

methyl	S^2_{axis}	τ_e (ps)	accessibility (Å^2)[a]	*B*-factor (Å^2)[b]
M0 ϵ	0.05 ± 0.01	8.5 ± 0.3	55.5, 104.9	–
V1 γ_1	0.28 ± 0.01	65.8 ± 1.7	0.0, 12.7	28.0
A3 β	0.85 ± 0.04	74.0 ± 3.4	17.6, 39.5	24.2
L5 δ_1	0.73 ± 0.07	90.9 ± 10.5	4.9, 34.3	17.5
L5 δ_2	0.78 ± 0.03	32.6 ± 2.7	4.9, 34.3	17.5
L10 δ_2	0.57 ± 0.02	25.3 ± 1.7	4.3, 4.4	29.6
V11 γ_1	0.48 ± 0.01	63.6 ± 2.1	24.5, 41.1	15.3
V11 γ_2	0.58 ± 0.02	80.2 ± 2.9	24.5, 41.1	15.3
M20 ϵ	0.95 ± 0.08	7.7 ± 2.7	0.0, 10.1	13.4
V25 γ_2	0.93 ± 0.07	15.8 ± 2.6	7.6, 5.7	17.7
A28 β	0.86 ± 0.01	51.9 ± 4.3	8.6, 54.5	21.0
T29 γ_2	0.30 ± 0.01	30.1 ± 1.3	1.3, 37.8	18.4
V32 γ_2	0.35 ± 0.03	84.7 ± 4.7	7.8, 49.4	28.0[c]
M35 ϵ	0.12 ± 0.01	8.1 ± 0.3	20.5, 140.8	30.7
T36 γ_2	0.52 ± 0.08	55.6 ± 12.4	4.4, 7.4	25.1[c]
T40 γ_2	0.17 ± 0.03	53.2 ± 4.2	0.0, 2.2	13.0
I41 δ_1	0.43 ± 0.01	15.9 ± 0.8	0.0, 30.9	16.0
I41 γ_2	0.89 ± 0.03	31.8 ± 1.6	0.0, 30.9	20.2
I42 γ_2	0.89 ± 0.03	24.2 ± 1.7	0.5, 0.0	15.6
I48 γ_2	0.86 ± 0.03	30.2 ± 1.3	0.7, 58.8	14.5
L49 δ_2	0.14 ± 0.01	34.2 ± 0.9	0.0, 2.4	24.7
L51 δ_1	0.28 ± 0.02	46.8 ± 2.1	0.0, 5.9	20.0
T56 γ_2	0.58 ± 0.05	45.8 ± 3.9	40.6, 107.8	25.4
I62 δ_1	0.80 ± 0.04	13.4 ± 1.9	5.6, 15.1	13.2
I62 γ_2	0.84 ± 0.03	40.6 ± 3.1	5.6, 15.1	15.1
L66 δ_1	0.79 ± 0.05	55.3 ± 3.8	17.1, 43.9	35.9
T74 γ_2	0.84 ± 0.48	32.3 ± 19.7	4.5, 3.5	12.0
A75 β	0.83 ± 0.13	68.1 ± 10.3	10.9, 36.0	13.6
V80 γ_1	0.90 ± 0.06	64.6 ± 5.8	2.8, 0.0	14.7[c]
V80 γ_2	0.94 ± 0.06	21.5 ± 3.3	2.8, 0.0	14.7[c]
I83 δ_1	0.61 ± 0.02	11.6 ± 0.9	0.3, 50.3	21.5
I83 γ_2	0.60 ± 0.02	41.5 ± 1.3	0.3, 50.3	16.8
V84 γ_2	0.99 ± 0.04	9.4 ± 1.9	0.0, 1.2	11.6
T85 γ_2	0.81 ± 0.06	67.4 ± 4.9	0.0, 50.3	26.6[c]
L91 δ_2	0.34 ± 0.02	81.7 ± 3.0	0.0, 0.3	23.0
V92 γ_1	0.93 ± 0.03	23.1 ± 1.4	0.4, 28.6	13.3
L94 δ_1	0.51 ± 0.01	38.3 ± 1.4	0.1, 31.4	22.4
T103 γ_2	0.57 ± 0.03	63.4 ± 2.9	0.1, 38.8	15.1
V105 γ_1	0.86 ± 0.03	51.3 ± 2.6	0.0, 25.7	14.3
V105 γ_2	0.86 ± 0.03	21.6 ± 1.5	0.0, 25.7	14.3
L108 δ_2	0.31 ± 0.02	41.4 ± 1.7	21.6, 25.3	25.0
I109 δ_1	0.40 ± 0.01	30.1 ± 1.1	2.4, 88.0	34.6
I109 γ_2	0.76 ± 0.02	29.1 ± 1.2	2.4, 88.0	31.7
L113 δ_1	0.27 ± 0.02	32.7 ± 1.7	0.0, 2.0	32.5[c]
L113 δ_2	0.25 ± 0.01	26.4 ± 1.0	0.0, 2.0	32.5[c]
I114 δ_1	0.32 ± 0.02	31.7 ± 1.5	0.0, 28.0	25.7
I114 γ_2	0.87 ± 0.04	24.9 ± 1.6	0.0, 28.0	14.8
L115 δ_2	0.88 ± 0.13	12.5 ± 7.0	0.0, 7.2	13.7
L117 δ_1	0.45 ± 0.09	47.4 ± 10.4	0.0, 7.2	20.6
T118 γ_2	0.86 ± 0.05	38.2 ± 3.2	0.7, 45.8	16.5
A122 β	0.98 ± 0.07	80.3 ± 6.3	7.1, 5.0	16.1
V123 γ_1	0.79 ± 0.02	51.8 ± 2.3	6.8, 66.8	19.5
A132 β	0.29 ± 0.01	31.6 ± 0.7	98.2, 60.2	–

[a] The first number is the accessible surface area for all backbone atoms, and the second number is the accessible surface area for all side chain atoms. These values were computed after adding hydrogen atoms and residues M0 and A132 to PDB entry 1HMT. [b] Temperature factors for the methyl carbon as given in PDB entry 1HMT. For V and L residues, the methyl carbon *B*-factors were averaged. [c] Residues with both major and minor conformers in PDB entry 1HMT.

A-LBP and M-FABP Side Chain Dynamics. Panels A and B of Figure 9 display the methyl S^2_{axis} values mapped onto the respective methyl groups of A-LBP and M-FABP. For both proteins, the methyl groups display a wide range of motional restriction on the picosecond to nanosecond time scale. There is some tendency for methyl groups with similar dynamic behavior to cluster spatially. Overall, little correlation exists between local side chain solvent accessibility and side chain disorder (as reflected in S^2_{axis}). For example, L91, which is essentially completely buried in both A-LBP and M-FABP, exhibits a highly disordered side chain in both proteins (Tables 2 and 3). T40, which is essentially completely buried in M-FABP, also displays a very low S^2_{axis} value (0.17 ± 0.03). However, on average, the δ- and ϵ-methyl groups display lower S^2_{axis} values than the β- and γ-methyls. If methyl groups from both A-LBP and M-FABP are included, S^2_{axis} values have been obtained for 10 β-methyls, 46 γ-methyls, 32 δ-methyls, and 7 ϵ-methyls. The average S^2_{axis} values for these methyls are 0.76 ± 0.21, 0.73 ± 0.20, 0.49 ± 0.21, and 0.38 ± 0.31, respectively. Also, one can predict, with reasonable confidence, high mobility for methyl groups at the ends of long, exposed side chains; e.g., the M35 ϵ-methyl in both proteins is highly mobile, as expected. Otherwise, we conclude that neither solvent accessibility nor side chain position is a reliable predictor of methyl group dynamic behavior. Kay and co-workers, in a study of the side chain dynamics of a Src homology 2 (SH2) domain (*32*), noted that a residue can be completely buried and yet still be quite mobile. Under certain circumstances, there may be multiple ways for side chains to pack together with extensive contacts. In such a situation, the favorable enthalpy of van der Waals contacts would be retained with higher conformational entropy compared to rigid packing. Interactions of this type have recently been termed "dynamic close packing" (*10*).

The *B*-factor values reported in Tables 2 and 3 have been taken from crystal structures that do not correspond exactly to human apo-A-LBP and human apo-M-FABP. Dynamical changes relative to the apo states of the human proteins may arise either from residue substitutions in the case of murine A-LBP or from stearate binding in the case of human M-FABP. Therefore, the *B*-factor data must be viewed with caution when comparisons are made to the ^{2}H relaxation results. Nevertheless, even with these caveats, the side chain atom *B*-factors do not appear to be reliable indicators of solution-state side chain dynamics.

In addition to *B*-factors, the existence of discrete conformations also provides evidence for side chain motions. Discrete conformations are displayed by residues V32, T36, T39, V80, T85, T102, L113, and T125 in the M-FABP crystal structures (*5*). V32, T36, and L113 have S^2_{axis} values consistent with multiple conformations, and V80 and T85 have S^2_{axis} values consistent with relatively rigid side chains. V80 and T85 may undergo conformational interconversions on time scales sufficiently long that the ^{2}H relaxation rates are not affected. T39, T102, and T125 have not been characterized.

There are several distinct dynamical differences between corresponding side chains within or near the binding pockets of A-LBP and M-FABP. For example, M20 is quite flexible in A-LBP (ϵ-methyl $S^2_{axis} = 0.43 \pm 0.02$), whereas it is rather rigid in M-FABP (ϵ-methyl $S^2_{axis} = 0.95 \pm 0.08$). In contrast, the spatially adjacent residue T29 is relatively rigid in A-LBP (γ_2-methyl $S^2_{axis} = 0.78 \pm 0.06$), but it is highly flexible in M-FABP (γ_2-methyl $S^2_{axis} = 0.30 \pm 0.06$). There are no obvious structural differences that can account for this result. I51 is relatively rigid in A-LBP (γ_2-methyl $S^2_{axis} = 0.95 \pm 0.05$, δ_1-methyl $S^2_{axis} = 0.78 \pm 0.04$), whereas L51 is highly flexible in M-FABP (δ_1-methyl $S^2_{axis} = 0.28$

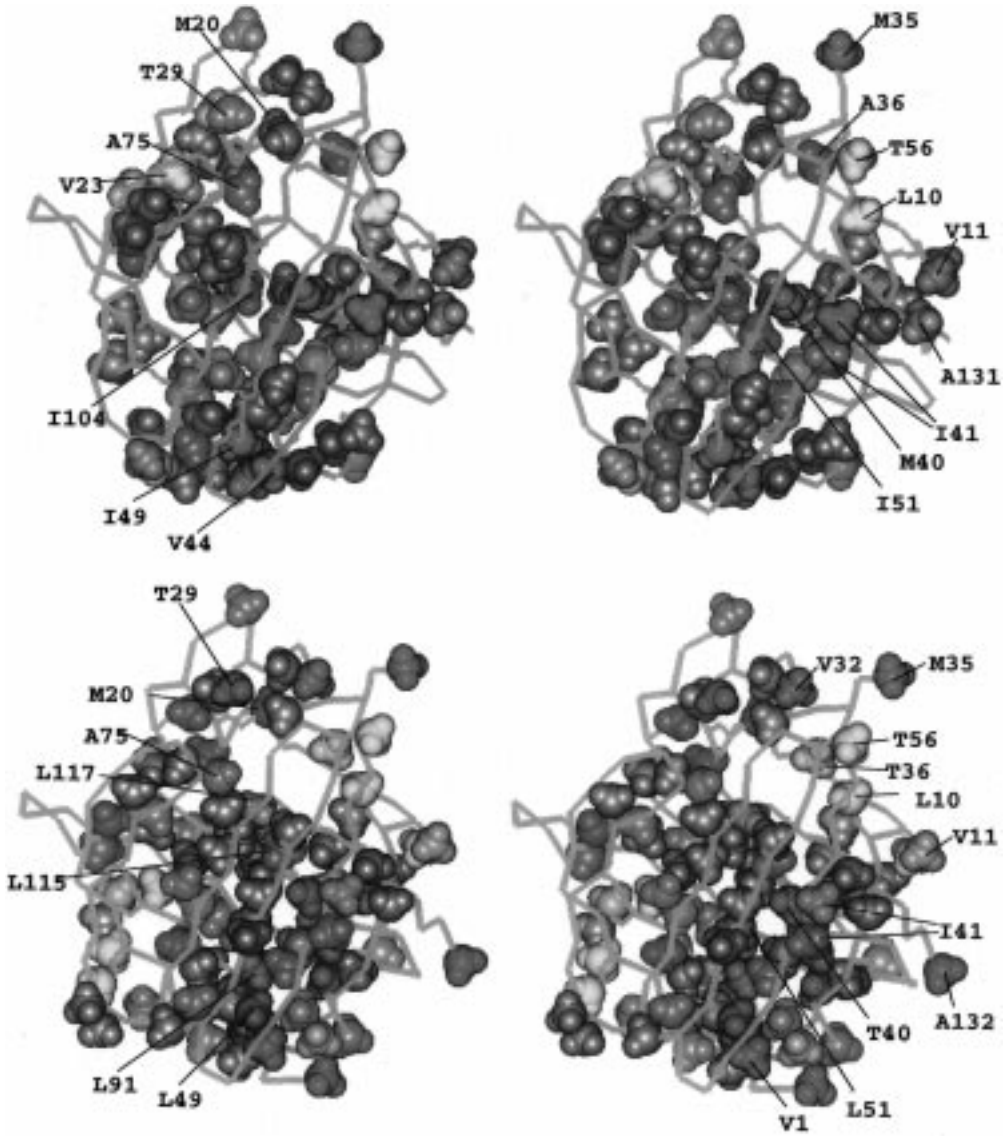

FIGURE 9: Stereoviews of side chain methyl group S^2_{axis} values mapped onto the protein structures. The C^{α} traces and non-methyl side chain heavy atoms are shown as gray sticks. All methyl groups are shown in a space-filling representation. Methyl groups for which no ^2H relaxation data could be obtained are shown in gray. The remaining methyl groups are color-coded as follows. Methyl groups with S^2_{axis} values of <0.30 are colored red. For the remaining characterized methyl groups, the color is scaled from red ($S^2_{axis} = 0.30$) to yellow ($S^2_{axis} = 0.65$) to blue ($S^2_{axis} = 1.00$). (A, top) Methyl S^2_{axis} values for A-LBP mapped onto the human A-LBP homology model, derived from PDB entry 1LIB. Selected residues are labeled. (B, bottom) Methyl S^2_{axis} values for M-FABP mapped onto the M-FABP X-ray structure (1HMT). Selected residues are labeled. These images were created using InsightII.

$\pm$ 0.02). Other less dramatic differences are also apparent (Tables 2 and 3).

Finally, we note that L115 in M-FABP is relatively rigid (δ_2-methyl $S^2_{axis} = 0.88 \pm 0.13$). Comparative ^2H relaxation data were not obtained for V115 in A-LBP. L115 in M-FABP is an important residue for two reasons. First, the side chain of L115 protrudes into the M-FABP binding pocket. Second, L115 is also one of the binding pocket residues that is substituted in A-LBP (V115). Both the larger volume occluded by a leucine residue relative to that of a valine and the rigidity of L115 in M-FABP suggest that this site, by way of steric hindrance, may play a role in defining differential ligand selectivity between A-LBP and M-FABP.

Implications for Ligand Selectivity. A comparison of the structures reveals the following sequence differences (A-LBP $\rightarrow$ M-FABP) in residues that lie within or near the binding pocket: V23 $\rightarrow$ L23, A36 $\rightarrow$ T36, M40 $\rightarrow$ T40, I51 $\rightarrow$ L51, S53 $\rightarrow$ T53, I104 $\rightarrow$ L104, V115 $\rightarrow$ L115, and C117 $\rightarrow$ L117. Several of the differences involve replacing a smaller residue in A-LBP with a larger residue in M-FABP. In general, this observation suggests that A-LBP-selective ligands may be the result of steric clashes with the larger residues in the M-FABP binding pocket. Alternatively, ligands that fit into the M-FABP binding pocket without steric clashes may show higher affinity for M-FABP due to more extensive contacts with binding site residues and smaller reductions in the conformational entropy of the portal region. This may help account for the generally higher affinity of M-FABP relative to that of A-LBP for natural fatty acids (*2*, *3*). In this context, we note that the binding of palmitate to I-FABP has been observed to increase the order of the highly flexible ligand entry portal (*6*). Furthermore, entropy changes associated with fatty acid binding are generally more negative for I-FABP compared to A-LBP and M-FABP (*77*).

The impact of a steric clash on ligand binding may depend on the relative rigidity and/or flexibility of the involved side chains. As such, the side chain dynamical properties described herein should have important consequences for both ligand binding and ligand selectivity. Flexible residues are more likely to adopt alternate conformations in response to the binding of different ligands, while rigid residues are more likely to clash sterically with ligands that bind with less than ideal fits.

CONCLUSIONS

The combined use of ^{15}N and ^{2}H relaxation measurements has afforded detailed characterizations of both the backbone and side chain dynamics of A-LBP and M-FABP. Our results, along with the published results for apo-I-FABP (*6*), demonstrate that iLPBs can display markedly different backbone dynamic behavior, particularly in the proposed ligand entry portal (*64*, *65*). A-LBP is significantly more mobile than M-FABP in the portal region on both the picosecond to nanosecond and microsecond to millisecond time scales. This property, along with the larger binding cavity in A-LBP relative to that in M-FABP, suggests that A-LBP should be more promiscuous in its ability to bind larger ligands. Although I-FABP is highly flexible (*6*), its specificity may be restricted by its relatively small cavity volume; the cavity volume of I-FABP is only 451 Å^3, whereas the cavity volume of A-LBP is 670 Å^3 (*1*). In general, our results indicate that differences in both structural and dynamical properties must be considered to fully account for differential ligand selectivities.

ACKNOWLEDGMENT

We thank Neil A. Farrow and Lewis E. Kay for providing software used in the analysis of the relaxation data. We also thank Dr. Kay for providing the basic pulse sequences used to measure the ^{2}H relaxation rates. We thank Ning Yan, Thomas Lavoie, and Bethanne Warrack for assisting in the N-terminal analyses.

SUPPORTING INFORMATION AVAILABLE

Descriptions of the acquisition and processing of the 3D spectra used to assign A-LBP and M-FABP, theoretical background, and tables listing the resonance assignments, ^{15}N relaxation parameters, ^{15}N model-free parameters, ^{15}N reduced spectral function values, and ^{2}H relaxation parameters (25 pages). Ordering information is given on any current masthead page.

REFERENCES

1. Banaszak, L., Winter, N., Xu, Z., Bernlohr, D. A., Cowan, S., and Jones, T. A. (1994) *Adv. Protein Chem. 45*, 89−151.
2. Richieri, G. V., Ogata, R. T., and Kleinfeld, A. M. (1994) *J. Biol. Chem. 269*, 23918−23930.
3. Richieri, G. V., Ogata, R. T., and Kleinfeld, A. M. (1996) *J. Biol. Chem. 271*, 11291−11300.
4. Xu, Z., Bernlohr, D., and Banaszak, L. J. (1993) *J. Biol. Chem. 268*, 7874−7884.
5. Young, A. C. M., Scapin, G., Kromminga, A., Patel, S. B., Veerkamp, J. H., and Sacchettini, J. C. (1994) *Structure 2*, 523−534.
6. Hodsdon, M. E., and Cistola, D. P. (1997) *Biochemistry 36*, 2278−2290.
7. Lücke, C., Zhang, F., Rüterjans, H., Hamilton, J. A., and Sacchettini, J. C. (1996) *Structure 4*, 785−800.
8. Ansari, A., Berendzen, J., Brown, S. F., Frauenfelder, H., Iben, I. E. T., Sauke, T. B., Shyamsunder, E., and Young, R. D. (1985) *Proc. Natl. Acad. Sci. U.S.A. 82*, 5000−5004.
9. Morton, A., and Matthews, B. W. (1995) *Biochemistry 34*, 8576−8588.
10. Rader, S. D., and Agard, D. A. (1997) *Protein Sci. 6*, 1375−1386.
11. Koshland, D. E., Jr. (1958) *Proc. Natl. Acad. Sci. U.S.A. 44*, 98.
12. Bruzzese, F. J., and Connelly, P. R. (1997) *Biochemistry 36*, 10428−10438.
13. Stites, W. E. (1997) *Chem. Rev. 97*, 1233−1250.
14. Kay, L. E., Torchia, D. A., and Bax, A. (1989) *Biochemistry 28*, 8972−8979.
15. Kördel, J., Skelton, N. J., Akke, M., Palmer, A. G., III, and Chazin, W. J. (1992) *Biochemistry 31*, 4856−4866.
16. Akke, M., Skelton, N. J., Kördel, J., Palmer, A. G., III, and Chazin, W. J. (1993) *Biochemistry 32*, 9832−9844.
17. Constantine, K. L., Friedrichs, M. S., Goldfarb, V., Jeffrey, P. D., Sheriff, S., and Mueller, L. (1993) *Proteins: Struct., Funct., Genet. 15*, 290−311.
18. Wagner, G. (1993) *Curr. Opin. Struct. Biol. 3*, 748−754.
19. Farrow, N. A., Muhandiram, R., Singer, A. U., Pascal, S. M., Kay, C. M., Gish, G., Shoelson, S. E., Pawson, T., Forman-Kay, J. D., and Kay, L. E. (1994) *Biochemistry 33*, 5984−6003.
20. Buck, M., Boyd, J., Redfield, C., MacKenzie, D. A., Jeenes, D. J., Archer, D. B., and Dobson, C. M. (1995) *Biochemistry 34*, 4041−4055.
21. Mandel, A. M., Akke, M., and Palmer, A. G., III (1995) *J. Mol. Biol. 246*, 144−163.
22. Lipari, G., and Szabo, A. (1982) *J. Am. Chem. Soc. 104*, 4546−4559.
23. Lipari, G., and Szabo, A. (1982) *J. Am. Chem. Soc. 104*, 4559−4570.
24. Clore, G. M., Szabo, A., Bax, A., Kay, L. E., Driscoll, P. C., and Gronenborn, A. M. (1990) *J. Am. Chem. Soc. 112*, 4989−4991.
25. Clore, G. M., Driscoll, P. C., Wingfield, P. T., and Gronenborn, A. M. (1990) *Biochemistry 29*, 7387−7401.
26. Farrow, N. A., Zhang, O., Forman-Kay, J. D., and Kay, L. E. (1995) *Biochemistry 34*, 868−878.
27. Farrow, N. A., Zhang, O., Szabo, A., Torchia, D. A., and Kay, L. E. (1995) *J. Biomol. NMR 6*, 153−162.
28. Ishima, R., and Nagayama, K. (1995) *J. Magn. Reson. B108*, 73−76.
29. Lefevre, J. F., Dayie, K. T., Peng, J. W., and Wagner, G. (1996) *Biochemistry 35*, 2674−2686.
30. Wyss, D. F., Dayie, K. T., and Wagner, G. (1997) *Protein Sci. 6*, 534−542.
31. Muhandiram, D. R., Yamazaki, T., Sykes, B. D., and Kay, L. E. (1995) *J. Am. Chem. Soc. 117*, 11536−11544.
32. Kay, L. E., Muhandiram, D. R., Farrow, N. A., Aubin, Y., and Forman-Kay, J. D. (1996) *Biochemistry 35*, 361−368.
33. Marion, D., Ikura, M., and Bax, A. (1989) *J. Magn. Reson. 84*, 425−430.
34. Skelton, N. J., Palmer, A. G., III, Akke, M., Kördel, J., Rance, M., and Chazin, W. J. (1993) *J. Magn. Reson. B102*, 253−264.
35. Bax, A., and Pochapsky, S. S. (1992) *J. Magn. Reson. 99*, 638−643.
36. Kay, L. E., Keifer, P., and Saarinen, T. (1992) *J. Am. Chem. Soc. 114*, 10663−10665.
37. Kay, L. E., Xu, G. Y., and Yamazaki, T. (1994) *J. Magn. Reson. A109*, 129−134.
38. Li, Y.-C., and Montelione, G. T. (1994) *J. Magn. Reson. B105*, 45−51.
39. Brown, S. C., Weber, P. L., and Mueller, L. (1988) *J. Magn. Reson. 77*, 166−169.
40. Friedrichs, M. S., Mueller, L., and Wittekind, M. (1994) *J. Biomol. NMR 4*, 703−726.

41. Constantine, K. L., Mueller, L., Goldfarb, V., Wittekind, M., Metzler, W. J., Yanchunas, J., Jr., Robertson, J. G., Malley, M. F., Friedrichs, M. S., and Farmer, B. T. (1997) *J. Mol. Biol. 267*, 1223−1246.
42. Friedrichs, M. S., Stouch, T. R., Bruccoleri, R. E., Mueller, L., and Constantine, K. L. (1995) *J. Am. Chem. Soc. 117*, 10855−10864.
43. Abragam, A. (1961) *Principles of Nuclear Magnetism*, Clarendon Press, Oxford, U.K.
44. Press, W. H., Flannery, B. P., Teukolsky, S. A., and Vetterling, W. T. (1989) *Numerical Recipies: The Art of Scientific Computing*, Cambridge University Press, Cambridge, U.K.
45. Markus, M. A., Dayie, K. T., Matsudaira, P., and Wagner, G. (1996) *Biochemistry 35*, 1722−1732.
46. Lee, C., and Subbiah, S. (1991) *J. Mol. Biol. 217*, 373−388.
47. Lee, C. (1994) *J. Mol. Biol. 236*, 918−939.
48. Brünger, A. T. (1992) *X-PLOR*, version 3.1, Yale University Press, New Haven, CT.
49. Lee, B., and Richards, F. M. (1971) *J. Mol. Biol. 55*, 379−400.
50. Lassen, D., Lücke, C., Kveder, M., Mesgarzadeh, A., Schmidt, J. M., Specht, B., Lezius, A., Spener, F., and Rüterjans, H. (1995) *Eur. J. Biochem. 230*, 266−280.
51. Hansen, A. P., Petros, A. M., Meadows, R. P., and Fesik, S. W. (1994) *Biochemistry 33*, 15418−15424.
52. Tjandra, N., Feller, S. E., Pastor, R. W., and Bax, A. (1995) *J. Am. Chem. Soc. 117*, 12562−12566.
53. Guenneugues, M., Drevet, P., Pinkasfeld, S., Gilquin, B., Menez, A., and Zinn-Justin, S. (1997) *Biochemistry 36*, 16097−16108.
54. Schurr, J. M., Babcock, H. P., and Fujimoto, B. S. (1994) *J. Magn. Reson. B105*, 211−224.
55. Tjandra, N., Wingfield, P., Stahl, S., and Bax, A. (1996) *J. Biomol. NMR 8*, 273−284.
56. Luginbühl, P., Pervushin, K. V., Iwai, H., and Wüthrich, K. (1997) *Biochemistry 36*, 7305−7312.
57. Barbato, G., Ikura, M., Kay, L. E., Pastor, R. W., and Bax, A. (1992) *Biochemistry 31*, 5269−5278.
58. Zink, T., Ross, A., Lüers, K., Cieslar, C., Rudolph, R., and Holak, T. (1994) *Biochemistry 33*, 8453−8463.
59. Brüschweiler, R., Liao, X., and Wright, P. E. (1995) *Science 268*, 886−889.
60. Mackay, J. P., Shaw, G. L., and King, G. F. (1996) *Biochemistry 35*, 4867−4877.
61. McEvoy, M. M., Muhandiram, D. R., Kay, L. E., and Dahlquist, F. W. (1996) *Biochemistry 35*, 5633−5640.
62. Zhou, H., McEvoy, M. M., Lowry, D. F., Swanson, R. V., Simon, M. I., and Dahlquist, F. W. (1996) *Biochemistry 35*, 433−443.
63. Jones, D. N. M., Searles, M. A., Shaw, G. L., Churchill, M. E. A., Ner, S. S., Keeler, J., Travers, A. A., and Neuhaus, D. (1994) *Structure 2*, 609−627.
64. Sacchettini, J. C., Gordon, J. I., and Banaszak, L. J. (1989) *J. Mol. Biol. 208*, 327−339.
65. Sacchettini, J. C., Scapin, G., Gopaul, D., and Gordon, J. I. (1992) *J. Biol. Chem 267*, 23534−23545.
66. Scapin, G., Gordon, J. I., and Sacchettini, J. C. (1992) *J. Biol. Chem. 267*, 4253−4269.
67. Daragan, V. A., and Mayo, K. H. (1997) *Prog. Nucl. Magn. Reson. Spectrosc. 31*, 63−105.
68. Szyperski, T., Luginbühl, P., Otting, G., and Wüthrich, K. (1993) *J. Biomol. NMR 3*, 151−164.
69. Orekhov, V. Y., Pervushin, K. V., and Arseniev, A. S. (1994) *Eur. J. Biochem. 219*, 887−896.
70. Tjandra, N., Kuboniwa, H., Ren, H., and Bax, A. (1995) *Eur. J. Biochem. 230*, 1014−1024.
71. Cistola, D. P., Kim, K., Rogl, H., and Frieden, C. (1996) *Biochemistry 35*, 7559−7565.
72. Carr, P. A., Erikson, H. P., and Palmer, A. G. (1997) *Structure 5*, 949−959.
73. Nicholson, L. K., Kay, L. E., Baldisseri, D. M., Arango, J., Young, P. E., Bax, A., and Torchia, D. A. (1992) *Biochemistry 31*, 5253−5263.
74. Palmer, A. G., III, Hochstrasser, R. A., Millar, D. P., Rance, M., and Wright, P. E. (1993) *J. Am. Chem. Soc. 115*, 6333−6345.
75. LeMaster, D. M., and Kushlan, D. M. (1996) *J. Am. Chem. Soc. 118*, 9255−9264.
76. Cavanagh, J., Fairbrother, W. J., Palmer, A. G., III, and Skelton, N. J. (1996) *Protein NMR Spectroscopy: Principles and Practice*, Academic Press, New York.
77. Richieri, G. V., Ogata, R. T., and Kleinfeld, A. M. (1995) *J. Biol. Chem. 270*, 15076−15084.

BI980203O